

Highlights

Analysis of Galactic cirrus filaments in HSC-SSP high-resolution deep images using artificial neural networks

Denis M. Poliakov, Anton A. Smirnov, Sergey S. Savchenko, Alexander A. Marchuk, Aleksandr V. Mosenkov, Vladimir B. Il'in, George A. Gontcharov, Daria G. Turichina, Andrey D. Panasyuk

- An ensemble of deep neural networks was used to identify cirrus in HSC-SSP data
- A catalog of cirrus filaments in deep optical HSC-SSP images has been created
- Cirrus clouds in HSC-SSP images agree well with cirrus in SDSS Stripe 82 images
- Large cirrus filaments may affect the quality of sky background estimation

Analysis of Galactic cirrus filaments in HSC-SSP high-resolution deep images using artificial neural networks

Denis M. Poliakov^{a,*}, Anton A. Smirnov^a, Sergey S. Savchenko^{a,b}, Alexander A. Marchuk^{a,b}, Aleksandr V. Mosenkov^c, Vladimir B. Il'in^{a,b}, George A. Gontcharov^a, Daria G. Turichina^{a,b}, Andrey D. Panasyuk^{a,b}

^a*Central (Pulkovo) Astronomical Observatory, Russian Academy of Sciences, Pulkovskoye chaussee 65/1, St. Petersburg, 196140, Russia*

^b*Saint Petersburg State University, Universitetskij pr. 28, St. Petersburg, 198504, Russia*

^c*Astrophysical Research Consortium, c/o Department of Astronomy, University of Washington, Box 351580, Seattle, WA 98195, USA*

Abstract

The existence of Galactic optical cirrus poses a challenge for observing faint objects within our Galaxy and dim extragalactic structures. To investigate individual cirrus filaments in the Hyper Suprime-Cam Subaru Strategic Program public data release 3 (HSC-SSP DR3) we use a technique based on convolutional neural networks and ensemble learning. This approach allows us to distinguish cirrus filaments from foreground and background objects across the entire HSC-SSP, using optical images in the g , r , and i wavebands. A comparison with previous work using deep Sloan Digital Sky Survey Stripe 82 (SDSS Stripe 82) data reveals that the cirrus clouds identified in this study are highly consistent in location within the overlapping survey region. However, in the deeper HSC-SSP dataset, we were able to detect 4.5 times more cirrus clouds. Our study indicates that the sky background in HSC-SSP coadd images is over-subtracted, as evidenced by the surface brightness distribution in cirrus filaments and surrounding regions. Objects with surface brightness of $m = 29$ mag arcsec $^{-2}$ near large filaments can be dimmed by over-subtraction of 0.5 magnitude in the r band. This suggests that cirrus clouds should be taken into account in algorithms for estimating the sky background. For practical use, we provide a catalog of filaments and a framework that allows one to train neural network models for segmenting cirri in HSC-SSP coadd images.

Keywords: methods: data analysis, catalogs, techniques: image processing, ISM: clouds, ISM: dust, extinction

1. Introduction

Cirrus clouds are diffuse filamentary structures resembling Earth's atmospheric cirrus clouds. Galactic cirri are observed predominantly at high Galactic latitudes ($b \gtrsim 20^\circ$) and have been identified in the infrared (IR) (Low et al., 1984; Kiss et al., 2001, 2003; Martin et al., 2010; Veneziani et al., 2010; Planck Collaboration et al., 2011; Pénin et al., 2012; Schisano et al., 2020), optical (de Vaucouleurs, 1955, 1960; de Vaucouleurs and Freeman, 1972; Sandage, 1976; Mattila, 1979; de Vries and Le Poole, 1985; Laureijs et al., 1987; Witt et al., 2008; Ienaka et al., 2013; Miville-Deschénes et al., 2016; Román et al., 2020; Gontcharov et al., 2022; Smirnov et al., 2023), and ultraviolet (Haikala et al., 1995; Witt et al., 1997; Gillmon and Shull, 2006; Boissier et al., 2015; Akshaya et al., 2019; Gontcharov et al., 2022). Various studies have also found that cirrus fluxes in the optical and IR spatially correlate with emission in lines of CO and H₂ (Weiland et al., 1986; de Vries et al., 1987; Gillmon and Shull, 2006; Ienaka et al., 2013; Román et al., 2020). At optical wavelengths, emission associated with Galactic cirrus directly contributes to diffuse Galactic light (DGL). This links the observed filamentary structures with the formation of sky background at high Galactic latitudes.

The DGL is a part of the sky background (light from diffuse and unresolved sources) that consists of starlight scattered by and re-emitted as thermal radiation from interstellar dust in the diffuse interstellar medium (ISM). The DGL was studied by Brandt and Draine (2012); Chellew et al. (2022), and it was found to be consistent with the light spectrum produced by a dust model of Zubko et al. (2004). A detailed study of the high Galactic latitude

*Corresponding author

Email address: polyakovdm193@gmail.com (Denis M. Poliakov)

translucent cloud MBM32 by Ienaka et al. (2013) found a correlation between emission at $100\ \mu\text{m}$ and intensity of the DGL. However, the slope of this correlation is twice that predicted by dust models (Weingartner and Draine, 2001; Zubko et al., 2004). MBM32 was also studied in Onishi et al. (2018) using near-IR observations at Science and Technology Satellite-3 (STSAT-3). The authors calculated the DGL spectrum from a recent model of Wang et al. (2015) and compared it with their observations. The comparison revealed that the observed color of near-IR DGL is closer to the model spectra without very large grains. Other cirrus clouds, called the Spider complex, were used by Bowes and Martin (2023); Zhang et al. (2023) to test new approaches to constraining the interstellar dust and anisotropic interstellar radiation field models required to interpret different cirrus observations. A number of studies (Bernard et al., 1994; Szomoru and Guhathakurta, 1998; Veneziani et al., 2010; Planck Collaboration et al., 2014; Bianchi et al., 2017) have investigated the relationship between the cirrus spectrum (emission and reflected spectra) and the properties of dust in filaments. These studies mainly used IR, microwave, and submillimeter data, except for Szomoru and Guhathakurta (1998), which used spectrographic data in the wavelength range $4090\ \text{\AA} - 9590\ \text{\AA}$. These investigations focus on the properties of dust and ISM, such as temperature, spectral index, emissivity, and opacity. In particular, consistent estimates of the dust temperature ($T \sim 20\ \text{K}$) in high-latitude Galactic cirri were obtained in Veneziani et al. (2010); Planck Collaboration et al. (2014); Bianchi et al. (2017).

The complex form of cirrus clouds has been the subject of extensive research. They are typically observed as groups of numerous co-directed filaments, rather than distinctly shaped clouds. The fractal nature of the cirrus has been identified and confirmed in various studies (Bazell and Desert, 1988; Falgarone et al., 1991; Hetem and Lepine, 1993; Vogelaar and Wakker, 1994; Elmegreen and Falgarone, 1996; Sánchez et al., 2005; Juvela et al., 2018; Marchuk et al., 2021). This morphological complexity makes the identification and segmentation of cirrus filaments a non-trivial task, particularly in deep wide-field imaging surveys. Such an appearance of these structures is believed to be a result of the diverse physical processes such as turbulence (Padoan et al., 2001; Kowal and Lazarian, 2007; Federrath et al., 2009; Konstandin et al., 2016; Beattie et al., 2019a,b), shock waves (Koyama and Inutsuka, 2000), cooling flows (Vazquez-Semadeni et al., 2007), the instability of a self-gravitating sheet (Nagai et al., 1998), and various instabilities in non-self-gravitating clumps, which arise because of the presence of magnetic fields (Hennebelle, 2013).

The investigation of these structures is important for studying various extragalactic sources (Cortese et al., 2010; Sollima et al., 2010; Rudick et al., 2010; Davies et al., 2010; Duc et al., 2018; Barrena et al., 2018), since cirri are found in both high and low Galactic latitudes (Barrena et al., 2018; Schisano et al., 2020; Román et al., 2020; Zhao et al., 2024). The presence of cirrus in deep images hinders the identification of background objects, such as faint galaxies and tidal features in interacting galaxies.

Catalogues of cirrus filaments, such as those presented by Schisano et al. (2020) and Smirnov et al. (2023), are essential for accounting for the impact of cirrus on the observed properties of extragalactic objects. Additionally, studying the optical properties of cirrus clouds can help distinguish them from extragalactic sources. Such investigation have been conducted in Román et al. (2020); Mattila et al. (2023) and in our recent work (Smirnov et al., 2023). Román et al. (2020) and Smirnov et al. (2023) focus in cirrus clouds in the Sloan Digital Sky Survey Stripe 82 (SDSS Stripe 82) region (Abazajian et al., 2009) and are based on deep images from SDSS Stripe 82 (Fliri and Trujillo, 2016). In Smirnov et al. (2023), we demonstrated that the colors of most detected filaments cluster around specific values and fall within the following ranges: $0.55 \leq g - r \leq 0.73$ and $0.01 \leq r - i \leq 0.33$. These results are largely consistent with those reported in Román et al. (2020), which were expressed as the inequality: $(r - i) < 0.43 \times (g - r) - 0.06$. Catalogues of cirrus filaments can also be utilized to determine interstellar extinction in cirrus. For instance, such estimations were conducted in Szomoru and Guhathakurta (1999); Gontcharov et al. (2022) using the star count method with Wolf diagrams (Wolf, 1923).

The creation of such catalogs on the scale of modern surveys requires robust and automated identification methods. Over the past decade, various methods have been employed to detect such structures. One approach was presented in Haigh et al. (2021), where the `NoiseChisel` (Akhlaghi and Ichikawa, 2015) and the `MTObjects` (Teenenga et al., 2013, 2016) tools, with Bayesian optimized parameters, were successfully used for cirrus detection in the Stripe 82 region. A different strategy was adopted by Schisano et al. (2020), where filaments in the Herschel infrared Galactic Plane Survey images (Molinari et al., 2010) were identified using a Hessian matrix. A similar method was used in Planck Collaboration et al. (2016) and Soler et al. (2022) to investigate the relative orientation between dust structures and the magnetic field, as well as between the HI filamentary structures and the Galactic disc, respectively. In Men'shchikov (2013), a multi-scale, multi-wavelength filament extraction method was proposed. In Salji et al. (2015), the authors developed and applied a Hessian-based ridge detection technique to extract filaments forming a

large “integral shaped filament” in Orion A North. To study cirrus in far-IR imaging data of dust emission released by the Herschel Gould Belt Survey team (André et al., 2010), a complex multistep method was employed in Koch and Rosolowsky (2015). This approach includes an arctan transformation of the image, Gaussian smoothing, adaptive thresholding, mathematical morphology (Serra and Serra, 1982), and the Rolling Hough Transform (Clark et al., 2014). The Rolling Hough Transform has also been used to remove cirrus from images obtained by the Dragonfly Telephoto Array (Danieli et al., 2020) in recent studies (Liu et al., 2022, 2025).

In recent years, neural networks have emerged as an effective tool for cirrus detection (Alina et al., 2022; Smirnov et al., 2023; Zavagno et al., 2023; Richards et al., 2024). Alina et al. (2022) showed the effectiveness of Mask R-CNN (He et al., 2017) and U-Net (Ronneberger et al., 2015) architectures in identifying cirri and determining their orientation using IR data from Planck and Herschel space observatories. Zavagno et al. (2023) based their research on the skeletons of filaments obtained in Schisano et al. (2020) and trained several neural networks using the U-Net and UNet++ (Zhou et al., 2018) architectures. Richards et al. (2024) proposed a gridded multi-scale architecture that uses three different attention modules, including a novel Gabor attention model. The architecture proposed in Richards et al. (2024) combines computational efficiency, high segmentation quality, and the ability to work with large images. In our recent work (Smirnov et al., 2023) we identified cirrus filaments using U-Net based neural network architectures in deep images from SDSS Stripe 82. Building upon this earlier work, the present study investigates cirrus filaments in optical images from the Hyper Suprime-Cam Subaru Strategic Program public data release 3 (HSC-SSP DR3, Aihara et al., 2022) using the neural network method developed in Smirnov et al. (2023). We aim to evaluate the performance of our neural network models on new data, compare the results with previous studies, and compile a catalog of cirrus filaments. As HSC-SSP images are deeper than SDSS Stripe 82 images and have a higher resolution, we hope to detect more cirrus clouds than in Smirnov et al. (2023).

The structure of this paper is as follows. In Section 2, we describe the data used and the preliminary steps required for identifying cirrus filaments and conducting their analysis. In Section 3, we give a description of the training dataset for the neural networks, their architecture, and the experimental results of their training. In Section 4, we present our main results. In Section 5, we describe the properties of the identified cirrus filaments and compare them with those of cirrus clouds reported in Smirnov et al. (2023), and then discuss the relationship between cirrus and background over-subtraction in the HSC-SSP data. We summarize our results in Section 6.

2. Data

In this work, we utilize deep images from the third data release of the HSC-SSP survey (Aihara et al., 2022). The largest component of this survey (the Wide layer) consists of three separate regions of the sky: two equatorial areas near the equinox points (“Fall equatorial field” and “Spring equatorial field”) and an area near the HectoMAP region (Geller et al., 2011) (“North field”). Hereafter, for convenience, we will refer to these regions as the Fall region, the Spring region, and the North region, respectively. A major advantage of the Fall region is its overlap with the SDSS Stripe 82 survey, which has been used to study cirrus in previous research (Román et al., 2020; Smirnov et al., 2023). This enables us to utilize previously obtained data for the overlapping region as a reference for investigating cirrus in the rest of the HSC-SSP survey, while also allowing for a comparison of cirrus parameters derived from the two independent datasets.

To achieve our goal of automatically detecting cirrus clouds, we utilize coadd optical images (the g, r, i bands) and masks in the r band. Since cirrus filaments are faint, diffuse objects, their detection and analysis are significantly impacted by aggressive sky subtraction (Borlaff et al., 2019). To address this issue, we use “global-sky” coadd images provided by HSC-SSP. The global sky subtraction technique in the HSC-SSP survey is designed to preserve the faintest extended features while minimizing over-subtraction around sources in the “global-sky” combined images. This technique was introduced in Aihara et al. (2019) and improved upon in Aihara et al. (2022). Unfortunately, this approach did not avoid sky over-subtraction around large cirrus filaments. Such contamination can clearly be seen in Fig. 1. The issue of sky over-subtraction is discussed in Section 5.2.

2.1. HSC-SSP DR3 images properties

The “global-sky” coadd images have a common photometric zero-point of 27.0 in broad bands (g, r, i, z, y , Aihara et al., 2018) and a pixel scale of 0.168 arcsec. The average 3σ surface brightness limits of the dataset $\mu_{\text{lim}}(3\sigma; 10) \times$



Figure 1: “global-sky” combined image of the Field f1053 in the r band. Contamination by sky over-subtraction is clearly seen in areas around cirrus filaments (darker areas).

$10'') = 30, 29.6, 29.4$ mag arcsec $^{-2}$ for the g , r , and i bands, respectively. We describe how these limits are calculated in Appendix A. According to Román et al. (2020), the corresponding brightness limits of SDSS Stripe 82 are: 29.1, 28.6, and 28.2 mag arcsec $^{-2}$. As a result, the HSC-SSP data are approximately 1 magnitude deeper than the SDSS Stripe 82 data.

To maintain compatibility with our previous work on the Stripe 82 survey, we chose to use the same tessellation scheme introduced in Section 3.1 of Fliri and Trujillo (2016), which is identical to the SDSS Stripe 82 scheme in the overlapping region. In this scheme, the celestial sphere is divided into separate fields with a step of 0.5 degrees in both declination and right ascension. Near the celestial equator, this results in nearly square fields with an area of 0.25 square degrees, while closer to the celestial poles, the fields become more elongated with a smaller area.

2.2. Preparing field images

The HSC-SSP survey provides many convenient Data Access Tools for HSC Data¹. Before being stacked into coadd images, the individual images were processed through the HSC pipeline. The description of this data processing pipeline can be found in Section 3 of Aihara et al. (2018). To download these “global-sky” coadd images and masks in FITS format, we used a command-line tool² as a Python module. This tool has an internal limit on the size of the image that can be requested, preventing the download of an entire field. To overcome this limitation, we requested overlapping image cutouts of $10.1' \times 10.1'$, with a stride of $10'$ between the centers of adjacent cutouts. If all nine image cutouts covering a field were available, we merged them into a single image of the field using the Swarp utility (Bertin et al., 2002). Since our approach to the automatic segmentation of cirrus clouds relies on images in the g , r , and i bands, we only considered fields with corresponding images available. The use of only three optical bands out of five available in the HSC-SSP DR3 (g , r , i , z , y bands) is due not only to the fact that these three bands were used in previous work (Smirnov et al., 2023), but also due to two other reasons. First, the usage of three bands allows us to cover about 1050 deg 2 . According Table 2 in Aihara et al. (2022), the full-color area (g , r , i , z , y bands) of the survey is only 670 deg 2 . Second, images in the g , r , i bands are considerably deeper than in z and y bands. According to Table 1 in Aihara et al. (2022), 5-sigma depths in g , r , i , z , y bands are 26.5 , 26.5 , 26.2 , 25.2 and 24.4 mag arcsec $^{-2}$, respectively. Therefore, the faint cirri in the images in the z , y bands will be less visible than those in the g , r , i bands.

Additionally, we used source masks in the r band. To prepare source masks, we used HSC-SSP masks in the r band. The HSC-SSP mask encodes the presence of certain objects or artifacts identified by the HSC-SSP pipeline using bits. A complete definition of all HSC-SSP mask bits can be found in the FITS file header. We specifically chose the fifth, eighth, and ninth bits corresponding to weak sources, “no-data” areas, and bright sources, respectively, to construct source masks. Thus, the source mask is a subset of the HSC-SSP mask.

A total of 4,331 fields in the HSC-SSP dataset are suitable for our analysis. For convenience, we divided the HSC-SSP data into five regions. Two of these correspond to the original HSC-SSP regions, namely the Spring and North regions (the frames of these regions are shown in Fig. 1 of Aihara et al. (2022)), while the remaining three are subdivisions of the HSC-SSP Fall region. The division scheme for the Fall region is illustrated in Fig.2. The location and number of fields in each region are provided in Table1.

2.3. Intersection dataset preparation

The first dataset we prepared consists of data from the intersection of the SDSS Stripe 82 region with HSC-SSP DR3 (hereafter referred to as the Intersection dataset). This dataset is used to train a neural network model for automatic cirrus segmentation and to compare the results with those from Smirnov et al. (2023). Stripe 82 is a narrow region of the sky, spanning 110 degrees in width ($-50^\circ < \alpha < 60^\circ$) and 2.5 degrees in height ($-1.25^\circ < \delta < 1.25^\circ$). The Intersection dataset contains 613 fields covering 153.25 deg 2 . Despite these fields being located close to the equator, their sizes differ slightly (the dimensions of the images along the x and y axes are in the range of 10715 – 10717 pixels). To enable a direct comparison of segmentation results with previous SDSS Stripe 82 data segmentation (Smirnov et al., 2023), the image sizes were reduced to 10715×10715 pixels by cropping pixels at the image border. The data preparation process outlined below in this section is shown in Fig. 3.

¹https://hsc-release.mtk.nao.ac.jp/doc/index.php/data-access_pdr3/

²<https://hsc-gitlab.mtk.nao.ac.jp/ssp-software/data-access-tools/-/tree/master/pdr3/downloadCutout/>

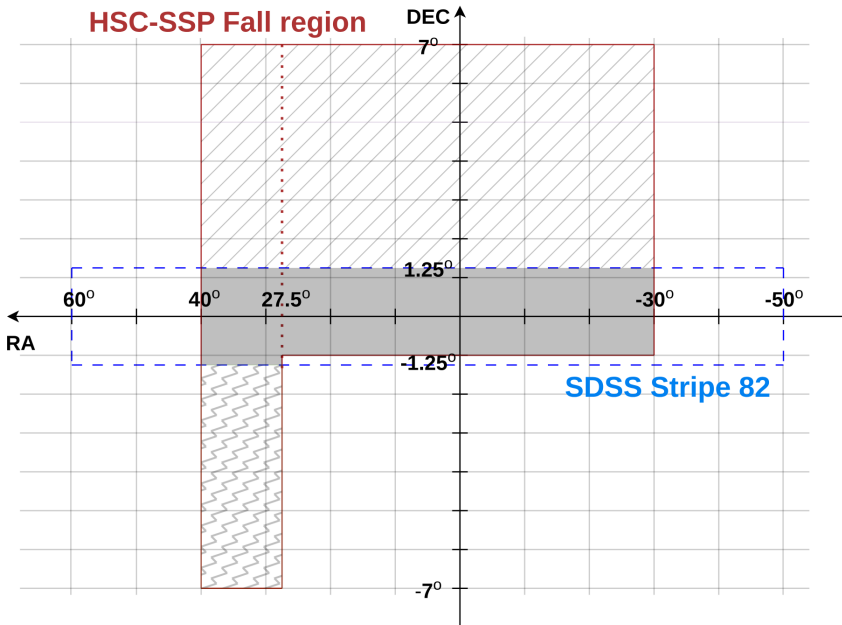


Figure 2: Schematic map of the HSC-SSP Fall region. The step of the coordinate grid along the DEC is 1° , and on the RA it is 10° . The SDSS Stripe 82 region is bounded by the dashed blue line. The HSC-SSP Fall region is bounded by the red solid line and divided into 3 regions. A hatched region is called the Fall plus region, a solid gray region is called the Intersection region, and a region filled with zigzag lines is called the Fall minus region.

In previous work (Smirnov et al., 2023), we used cleaned images in the r band to prepare a dataset for neural network training. Bright sources were masked in these images (cirrus filaments were left unmasked), and the background was interpolated inside the masked areas. Since one of the objectives of this study is to assess the impact of using cleaned images directly in a dataset for neural network training, we have also prepared cleaned images in the r band.

The first step in preparing the cleaned images was to mask out all objects in the images except cirrus. The prepared source masks cover all objects as well as some image artifacts. Although these masks cover the vast majority of objects, some, particularly extended ones, have faint outer wings that extend beyond the masked regions. To quantify the impact of these unmasked wings we have measured the surface brightness in a pixel-wide layers along the mask edges and found out that in r -band the median value for fifty random fields is $28.32 \text{ mag arcsec}^{-2}$, and top (brightest) quartile is $28.16 \text{ mag arcsec}^{-2}$, which is not negligible taken the survey depths. To solve this problem, we utilized mask images previously prepared in Smirnov et al. (2023) to train a conditional Generative Adversarial Network (GAN) (Goodfellow et al., 2014) for generating new masks. The GAN architecture consists of two networks: the generator and the discriminator. These networks are trained to compete with each other. In our case, the generator takes a field image as input and creates a mask image, while the discriminator distinguishes between real and generated masks. For our generator, we use the U-Net architecture (Ronneberger et al., 2015), while for the discriminator, we use a convolutional neural network with four convolutional blocks (two-dimensional convolution, batch normalization, and leaky ReLU activation) with 64, 128, 256 and 512 kernels. For the training purposes, we used the overlapping regions of SDSS Stripe 82 and HSC-SSP DR3 (Intersection region) to create 4500 training and 2500 testing samples. After completing the training, we generated new masks (“neural” masks) for all HSC-SSP DR3 images. As these masks are based on those from Smirnov et al., 2023, they cover all sources in the HSC-SSP images, regardless of their type. Cirrus filaments that overlap with sources are masked out, but those that are not overlapped with other sources are not. As the final masks of the background objects, we used a union of the source masks prepared with HSC-SSP masks and our neural masks. Hereafter, we refer to these masks as the “combined” masks. When we measured the surface brightness along the pixel-wide edges of our combined masks we found values which are lower by about 0.5 of a magnitude and with considerably lower scatter between fields: the median value is $28.86 \text{ mag arcsec}^{-2}$ and

Table 1: List of regions in the HSC-SSP survey. The first column contains the names of the regions. The range of coordinates that defines the approximate boundaries of each HSC-SSP region is contained in the second column, the area of each region is given in the round brackets. The third column gives the number of fields in each region, for which there are images in g , r , i bands.

Region name	(RA, Dec)	Number of fields
Intersection region	$-30^\circ \leq \text{RA} \leq 40^\circ, -1.25^\circ \leq \text{Dec.} \leq 1.25^\circ$ ($\simeq 160 \text{ deg}^2$)	613
Fall plus region	$-30^\circ \leq \text{RA} \leq 40^\circ, 1.25^\circ \leq \text{Dec.} \leq 7^\circ$ ($\simeq 400 \text{ deg}^2$)	613
Fall minus region	$27.5^\circ \leq \text{RA} \leq 40^\circ, -7^\circ \leq \text{Dec.} \leq -1.25^\circ$ ($\simeq 70 \text{ deg}^2$)	253
Spring region	$127.5^\circ \leq \text{RA} \leq 232.5^\circ, -2^\circ \leq \text{Dec.} \leq 5^\circ$ ($\simeq 730 \text{ deg}^2$)	2442
North region	$200^\circ \leq \text{RA} \leq 250^\circ, 42^\circ \leq \text{Dec.} \leq 44.5^\circ$ ($\simeq 90 \text{ deg}^2$)	410

the top (brightest) quartile is $28.75 \text{ mag arcsec}^{-2}$, which means that these new masks cover the background sources considerably better than the original ones.

To obtain cleaned images, i.e. images where all the background objects except cirri are cleaned out, we use the following procedure. For each masked region of our combined mask we zero-out all the pixels from the corresponding area of an r -band image. Then we fill this gap by interpolating the fluxes of a boundary layer of this masked region back to its center. To suppress the random noise during this interpolation we use four pixel wide boundary layer and apply a median filter to it.

Training a neural network segmentation model requires field images along with corresponding segmentation maps (pixel-wise labels). The creation of accurate cirrus segmentation maps, hereafter referred to as *cirrus maps*, is a complex and time-consuming task. The process of preparing cirrus maps is described below.

In our previous work (see Section 2.2 in Smirnov et al., 2023), we developed a semi-automatic method for preparing cirrus maps. Using this method, we have prepared a training dataset, the same size as in the previous work (see Section 3.1 in Smirnov et al., 2023). Unfortunately, the models trained on this dataset reached a low intersection over union metric ≤ 0.2 (Jaccard, 1901). Intersection over union metric (IoU) quantifies the degree of overlap between the predicted and actual cirrus map. For comparison, the best model yielded an IoU of 0.576 in Smirnov et al. (2023). We assume that our IoU is lower due to both the properties of the data and the quality of the cirrus maps. Indeed, careful visual inspection showed that the cirrus maps do not accurately reproduce the filament boundaries in the HSC-SSP DR3 images. Training a high-quality machine learning segmentation model using such a map is practically impossible. To create more accurate cirrus maps, we decided to use the DS9 contour tool (Joye and Mandel, 2003). We generated contours at $29 \text{ mag arcsec}^{-2}$ in the r band, using a smoothness parameter of 4, in images rescaled to 2143×2143 pixels. The choice of this isophote level is based on its use in our previous study (Smirnov et al., 2023). We manually selected those contours that correspond to the cirrus filaments. Then, in the selected filaments, we manually removed the brightest sources, such as stars and galaxies, as well as artifacts. Although this approach is more time-consuming than the semi-automatic method used in our previous work, it creates more accurate and detailed cirrus maps. Models trained on such maps yield larger IoU metric (see Section 3.3).

Using the method described above, we prepared cirrus maps for 70 randomly selected fields out of a total of 613. Although this is five times fewer than in our previous work, it proved sufficient for training and testing neural network models, which produced acceptable cirrus map quality (see Section 3). The cirrus maps for each field are stored in corresponding FITS files, where a pixel value of 0 represents the background, and 1 indicates cirrus. The fraction of pixels that denote cirrus in a field or region is referred to as the *cirrus fraction*.

As a final remark, it is worth noting that the original HSC-SSP data is affected by sky over-subtraction. This can be clearly seen in Fig. 1. Therefore, any pipeline that uses this data will inherit this flaw, including our manual cirrus maps. An important point is that our ultimate goal is to identify cirrus in contaminated data. Therefore, our neural network models should be trained on such data without the need for any additional sky over-subtraction correction. We further discuss sky over-subtraction in Section 5.2.

3. Automatic Cirrus Segmentation

Since the neural network architectures in our previous work (see Section 3.2 in Smirnov et al., 2023) effectively solved the problem of cirrus segmentation (cirrus map generation), we apply the same architectures to the HSC-SSP

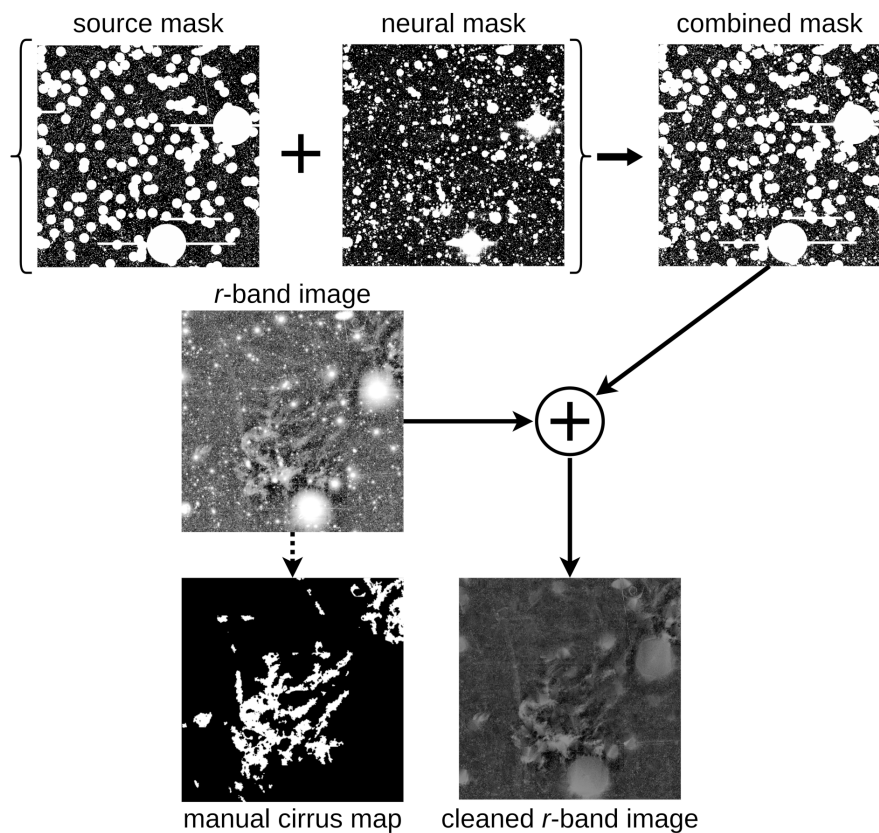


Figure 3: Diagram of the Intersection dataset preparation process. The top row of the diagram demonstrates the creation of a combined mask by the union of a neural mask and a source mask. The direct sum sign denotes the creation of a cleaned image in the r band from an image in the same band with a combined mask. The dotted arrow demonstrates the creation of a cirrus map using manually selected and corrected contours in DS9.

DR3 data. Improvements to the cirrus segmentation approach involve enhancements in data preprocessing and the use of model ensembles. In this section, we describe the dataset for neural network training, the network architecture, training methods, and the analysis of the trained models.

3.1. Training data for neural networks

In Section 2, we described the manual identification process for cirrus filaments. Here, we further process the segmentation data to train a neural network. Due to size limitations of neural network models, we use smaller square image fragments (windows) instead of the original large field images (10715×10715 pixels) during the training. This approach reduces computational time, memory usage, and the amount of manually annotated data required for neural network training. The 3- or 4-channel input images for the neural network are formed from the windows in the g , r , i bands and the windows from the cleaned images in the r band (fourth channel). Training a neural network requires dividing the data into three subsets: training, validation, and test sets. To form these subsets, we randomly selected three separate groups of fields, consisting of 37, 13 and 20 fields, respectively. Below, we outline the key steps for preprocessing the training and validation data.

1. We calculate the common 99.9th percentile and 0.1th percentile values for each band used (g , r , i and, if necessary, cleaned images in the r band) separately for all training and validation fields (50 fields). We then apply corresponding clipping (Berry and Burnell, 2005; Howell, 2006; Gonzalez and Woods, 2006) to moderate the effects of extremely bright pixels and over-subtraction near extended sources, which reduces image contrast. This clipping moderately increases the IoU of trained models (improvement is from 0.05 to 0.1 for different model parameters). Notably, in contrast to our previous work Smirnov et al. (2023), we use 0.1th percentile clipping instead of negative value clipping. This adjustment is necessary because over-subtraction occurs in areas near cirrus in HSC-SSP images, an artifact we will demonstrate in Section 5.2.
2. Next, we apply a natural logarithm transformation.
3. Then, we randomly choose n_{tr} square windows ($w \times w$ pixels) for each field in the training subset and n_{val} for each field in the validation subset. After that, we resize each window to match the spatial shape of the input tensor (w_{in} , w_{in}), using `cv2.resize` method with `cv2.INTER_LINEAR` interpolation from OpenCV library (Bradski, 2000).
4. The corresponding windows with the cirrus map are obtained from the files with the cirrus map and then resized, using `cv2.INTER_AREA` interpolation.
5. Finally, during the creation of the input tensor, we apply min-max normalization to the $[-1 : 1]$ range and augment the data by a symmetry group of the square. This group consists of $\pi/2$ rotations, reflections, and their compositions (eight elements). As a result, this procedure increases the number of windows by a factor of 8.

3.2. Network architecture and training methods

To generate cirrus maps, we employed the same network architecture used in our previous study on cirrus in SDSS Stripe 82 (Smirnov et al., 2023). This architecture is based on the encoder-decoder U-Net network (Ronneberger et al., 2015). Fig. 4 shows a visual representation of the neural network architecture used. As an encoder, we used MobileNetV2 (Sandler et al., 2018), as the models with it showed the highest IoU.

For each model under consideration, we used a sparse categorical cross-entropy loss function derived from the logits output tensor. For loss function optimization, we utilized the Adam optimizer (Kingma and Ba, 2014) with different learning rates r .

During the training experiments, we varied some parameters that influence the optimization process and the final model performance: the number of input channels n_{ch} (three or four), the scale factor s between the window size w and the input tensor spatial size w_{in} ($w = sw_{\text{in}}$), class weights $\overline{\omega}_c$, etc.

To train our network models, we used a single NVIDIA GeForce RTX 3060 GPU. The batches consisted of six windows for all models. To estimate a sufficient number of learning epochs, we trained 12 4-channel models for 100 epochs. The validation loss curves for these models are presented in Appendix B. The average value of the epoch in which the minimum validation loss was achieved was 12.2, with a standard deviation of 4.8 and a maximum of 19. Thus, to save time on training models, we decided to use 20 epochs for the remaining models. We used $w_{\text{in}} = 448$ for all the models considered. Since the size of the dataset is small, we used a different number of random windows from

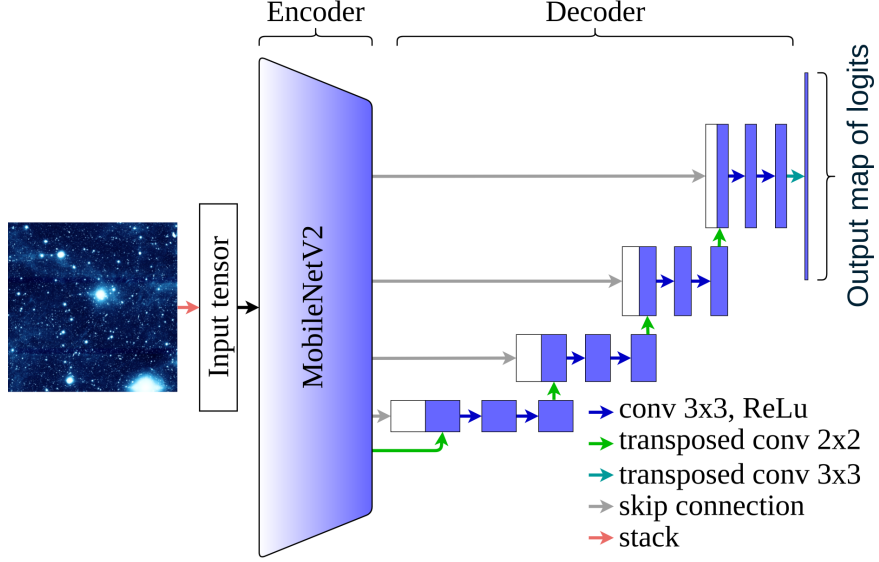


Figure 4: The encoder-decoder architecture used for creating cirrus maps.

each field in training and validation datasets (n_{tr} , n_{val}) for different values of s . For scale factors $s = 2$ and 4, we used $n_{\text{tr}} = 200$ and $n_{\text{val}} = 250$. For $s = 8$, we used $n_{\text{tr}} = 80$ and $n_{\text{val}} = 100$. The training time for a single model ranged from 6 to 15 hours.

The code used to train the segmentation models and produce the cirrus maps is available at https://gitlab.com/polyakovdmi93/cirrus_narrow_segmentation³.

3.3. Experimental results analysis

In this section, we describe experiments aimed at finding a more effective solution for generating cirrus maps. To assess the performance of different models, we employ the IoU metric. First, we compare the effectiveness of 3-channel and 4-channel models.

As can be seen from Tables C.4 and C.5, the metrics of models with identical parameters may differ by more than 0.1. This is probably due to the small size of the dataset. To compare 3-channel and 4-channel models, we compared their efficiency with intermediate class weights (1.0, 15.0). This allowed us to reduce the training time for 3-channel models. The average IoU value for 12 3-channel models, presented in Table C.4, is 0.3606 and the average IoU value for corresponding 4-channel models from Table C.5 is 0.363. Such a negligible difference in relation to the variation of the IoU of models with the same parameters indicates a similar quality of the 3-channel and 4-channel models.

Given the limited size of the training dataset, we explored the fine-tuning (Yin et al., 2017) of models trained in Smirnov et al. (2023) for cirrus map generation in SDSS Stripe 82 data. These models use 3-channel images. Each channel corresponds to an image in the g , r , i bands. Since the HSC-SSP survey includes the same optical bands as SDSS Stripe 82, we hypothesized that fine-tuning these models might allow us to create cirrus maps for the HSC-SSP survey data.

As a basic model for fine-tuning, we employed the most efficient model from Smirnov et al. (2023), which demonstrated an IoU of 0.576. This model creates a cirrus map using 3-channel images, sliding window size $w = 448$, scale factor $s = 1$ between the sliding window size w and the input tensor spatial size w_{in} ($w = sw_{\text{in}}$). The pixel scale in SDSS Stripe 82 is 0.396 arcsec, which differs from the HSC-SSP pixel scale of 0.168 arcsec. To address this difference in pixel scale, we conducted several fine-tuning experiments using scale factors of $s = 2$ and $s = 3$ (see Table C.6). Unfortunately, as can be seen from Tables C.5 and C.6, fine-tuned models did not achieve the same high IoU metrics

³The best way to use and modify this project is to create a fork after gaining access upon request.

N_{models}	IoU	precision	recall
3	0.479	0.687	0.612
5	0.477	0.7	0.599
7	0.475	0.679	0.612
9	0.48	0.686	0.616

Table 2: The metrics of the ensembles used. It lists IoU, precision, and recall for all test fields for the cirrus class. The first column contains the number of the best models in each ensemble. The maximum value of the IoU is highlighted in bold.

as models that are trained from scratch. This suggests a difference in the appearance of cirrus between SDSS Stripe 82 and HSC-SSP, which hinders effective fine-tuning. We infer that differences in image depth and data processing between the surveys (Sect. 2.1) are the primary factors contributing to the dissimilarity in cirrus appearance. These differences are demonstrated in Section 4.2.

In our previous work on cirrus in SDSS Stripe 82, the best model achieved an IoU of 0.576. This value is significantly higher than that of the best model in the current work (see Table C.5). To improve the results, we tried using ensembles of several top 4-channel models available. Each model in the ensemble produces its own independent cirrus map. These maps are combined into a final map using direct pixel-by-pixel majority voting. The use of an ensemble of models is a highly effective method to improve the performance of machine learning algorithms (Breiman, 1996; Friedman et al., 2000; Breiman, 2001; Ren et al., 2016; Mienye and Sun, 2022). This approach is used to solve problems related to classification, recognition, detection, and segmentation in various scientific fields. Ensembles are widely employed in medical research (Qurat-Ul-Ain et al., 2010; Fraz et al., 2012; Moradi et al., 2023; Tang et al., 2023), astronomy (Nun et al., 2016; Priyadarshini and Puri, 2021; Marchuk et al., 2022; Pagliaro et al., 2023; Savchenko et al., 2024; Zeraatgari et al., 2024), and other fields (Cyganek, 2012; Stork et al., 2012; Guan et al., 2013; Kinattukara and Verma, 2014; Nanni et al., 2023). We tested ensembles of three, five, seven and nine top 4-channel models (see Table 2). All considered ensembles of models show higher IoU compared to individual models. The best ensemble, consisting of nine models, achieves an IoU of 0.48 and is used for cirrus map generation further in this work.

We summarize the improvements to our cirrus map generation approach and the results of model training experiments as follows.

1. To adapt our previous approach to the new HSC-SSP data, we incorporated 0.1th percentile clipping in image preprocessing, which allows us to increase contrast in fields rich with cirrus.
2. We added the capability to train cirrus map generation models using 4-channel images. A comparison between 3-channel and 4-channel models revealed that, given the current problem and dataset size, both models exhibit similar IoU metrics. To better assess this similarity, a larger training sample is required.
3. We conducted several experiments to find a more effective model. As one can see in Table C.5, the highest IoU of a single model is 0.436. It is also worth noting that the reliability of these estimates is low due to the small test sample, which consists of only 20 fields.
4. We also conducted experiments to fine-tune the best model from Smirnov et al. (2023). Unfortunately, as shown in Tables C.5 and C.6, the fine-tuned models demonstrated lower performance than models trained from scratch.
5. To improve the quality of cirrus map generation, we utilized an ensemble of nine best 4-channel models, achieving an IoU of 0.48 for cirrus.

In the following sections, we use the cirrus maps obtained by using an ensemble of nine best 4-channel models. A diagram of the prediction of the cirrus map by this ensemble is shown in Fig. 5.

4. Results

In this section, we describe the identified cirrus in each of the HSC-SSP fields under consideration. The key questions we address are: What is the total area covered by cirrus? and What are its physical properties, such as surface brightness and typical sizes?

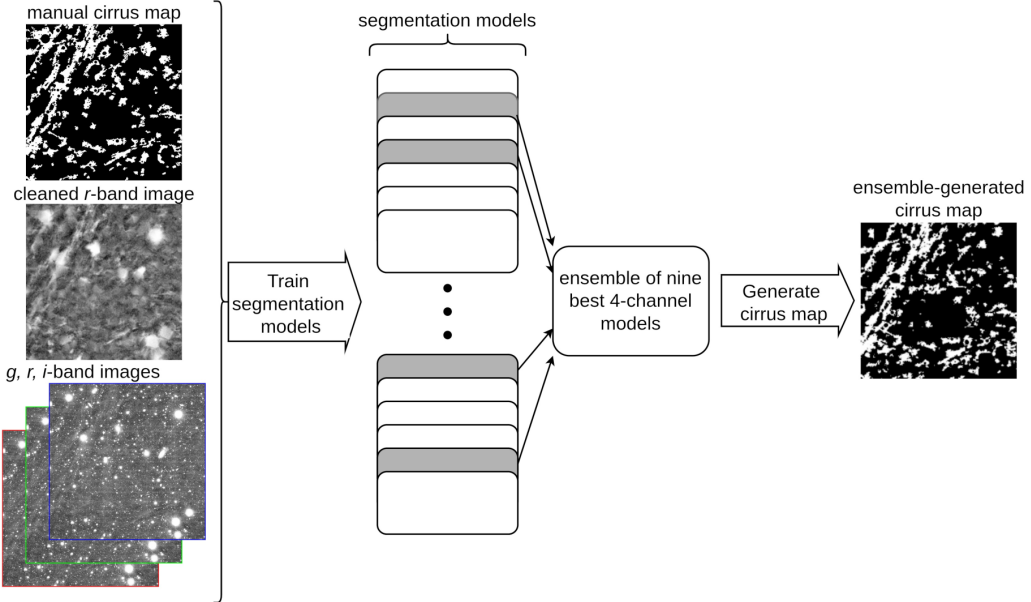


Figure 5: Diagram of the prediction of the cirrus map by the ensemble of nine best 4-channel models. In the left part of the diagram, the data used for model training is shown. It consists of ground-truth cirrus map created using manually selected and corrected contours in DS9 (manual cirrus map) and images from which the input tensor is formed (cleaned r -band image and images in g , r , i bands). Rounded rectangles in the central part of the diagram denote trained models. Gray rounded rectangles denote the best nine models selected for the ensemble. The arrow in the right part of the diagram represents the generation of a cirrus map through direct pixel-by-pixel majority voting by ensemble models.

4.1. Cirrus maps post processing

Although the ensemble method produces higher-quality cirrus maps compared to individual models, visual inspection reveals some false cirrus detections. Many of these false detections in HSC-SSP images are due to artifacts. An example of such an artifact is the complex pattern of scattered light, which is clearly visible in Fig. 6. To rectify the ensemble-generated cirrus maps, we manually removed individual artifacts. If a cirrus filament is partially overlapped by an artifact, the intersection is removed. We performed this procedure on fields where the cirrus fraction exceeded 0.5% (1689 out of 4331 fields). These fields account for 95.1% of the cirrus area annotated by the ensemble. False cirrus detections were found in 513 out of the 1689 fields considered.

The cirrus fraction in the ensemble-generated maps is 1.985%. After removing false cirrus detections, it decreased to 1.884%, indicating that false cirrus accounted for 0.101% of the total area of the considered fields. The cirrus fractions before and after rectification in each region of the HSC-SSP are presented in Table 3. Despite the small fraction of false cirrus, removing false detections allowed us to obtain more reliable cirrus properties. Therefore, in all subsequent sections, we use rectified cirrus maps.

Region name	f_{ens}	f_{rect}	f_{false}	$f_{\text{false}} / f_{\text{ens}}$
Intersection region	0.0434	0.0408	0.0026	0.06
Fall plus region	0.0463	0.0454	0.0008	<i>0.016</i>
Fall minus region	0.0046	0.0041	<i>0.0004</i>	0.09
Spring region	0.0109	0.0101	0.0008	0.07
North region	0.0034	0.0025	0.0008	0.247

Table 3: Cirrus fractions and false cirrus fractions in HSC-SSP regions. The first column contains the names of the regions. Cirrus fractions in ensemble-generated maps for regions are given in the f_{ens} column. The f_{rect} column shows cirrus fractions after false cirrus removing, fractions of false cirrus are contained in the f_{false} column ($f_{\text{false}} \equiv f_{\text{ens}} - f_{\text{rect}}$). The last column shows the proportion between false cirrus and cirrus annotated by the ensemble. The maximum and minimum values in the columns are highlighted in bold and italic, respectively.

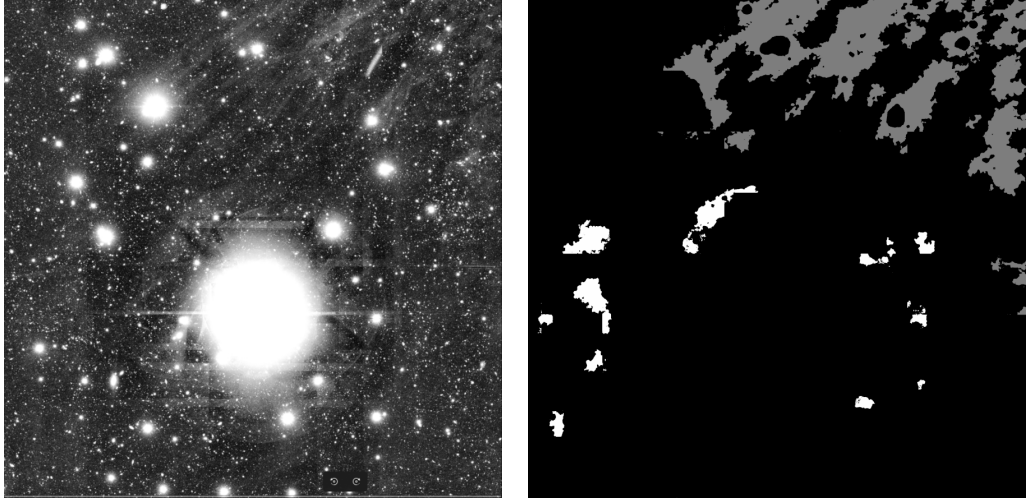


Figure 6: The left panel shows a part of the Field f0865 in the r band. The corresponding cirrus map with false cirrus detections is shown in the right panel. White pixels represent removed false cirrus detections. Gray pixels indicate remaining cirrus filaments.

The rectified cirrus maps that we generated may be useful to other researchers, so we have placed them in cloud storage. A detailed description of the data format and a link to the storage are available in our [GitLab](#) repository⁴.

4.2. Cirrus maps in Intersection region

A cirrus map of the Intersection region was previously generated in our work (Smirnov et al., 2023) using Stripe 82 data. Here, we examine the consistency between that map and a newly created HSC-SSP-based map from the present study. According to Table 3, the cirrus fraction in the HSC-SSP map for the Intersection region is $f_{\text{HSC-SSP}} = 0.0408$, whereas in the SDSS Stripe 82 map, it is $f_{\text{S82}} = 0.0092$. This advantage of HSC-SSP over SDSS Stripe 82 in the detected cirrus fraction can be attributed to the greater depth of HSC-SSP data compared to SDSS Stripe 82 data, allowing for the detection of fainter cirrus structures. The difference in the appearance of cirrus and the fraction of cirrus detected in HSC-SSP data and SDSS Stripe 82 data can be seen in Fig. 7. However, the consistency between these cirrus maps can be assessed using their $\text{IoU} = 0.105$. While this value may seem low, it aligns with the theoretical maximum, which is determined by the ratio of the cirrus fractions in the two maps: $\text{IoU}_{\text{max}} = f_{\text{S82}}/f_{\text{HSC-SSP}} = 0.225$. IoU_{max} is achieved when all cirrus detected in the Stripe 82 map are fully contained within the cirrus regions identified in the HSC-SSP map. We also compare the actual IoU with random IoU (IoU_{rand}). Random IoU is the IoU for maps consisting of 10^4 pairs of random non-equal fields (for any pair $\text{Field}_i, \text{Field}_j, i \neq j$) from the Intersection region. The first map consists of SDSS Stripe 82 cirrus maps for the first fields in each pair, while the second map contains HSC-SSP cirrus maps for the second fields in each pair. The IoU_{rand} corresponds to the degree of similarity between random maps from SDSS Stripe 82 and HSC-SSP. Since IoU_{rand} depends on choosing random pairs of maps, we repeated the calculation 100 times to get a sample distribution of IoU_{rand} . The average sample value $\langle \text{IoU}_{\text{rand}} \rangle = 0.0076$ and the sample standard deviation $\text{sd}(\text{IoU}_{\text{rand}}) = 0.0004$. The $\langle \text{IoU}_{\text{rand}} \rangle$ is significantly lower than the actual IoU , indicating a strong agreement between the cirrus map from Smirnov et al. (2023) and the newly generated map.

The spatial distribution of cirrus filaments over each HSC-SSP region after rebinning to a bin of 1 degree in right ascension and 0.5 degree in declination is presented in Figs. 8 and 9. The maps were obtained by summing the areas covered by cirrus in the corresponding fields and then rebinning the resulting values into bins of 1 deg in right ascension and 0.5 deg in declination, assuming that the cirrus should be assigned to a bin if the center of its field lies within that bin. First of all, as evident from these maps, the cirrus distribution across the sky is highly uneven (note the logarithmic scale of the colorbar). In the Intersection and the Fall regions, a large cirrus cloud is present on the right side of the region, covering α from -2^h to 0^h and δ from 0° to 7° , with the highest cirrus concentration around

⁴https://gitlab.com/polyakovdmi93/cirrus_narrow_segmentation

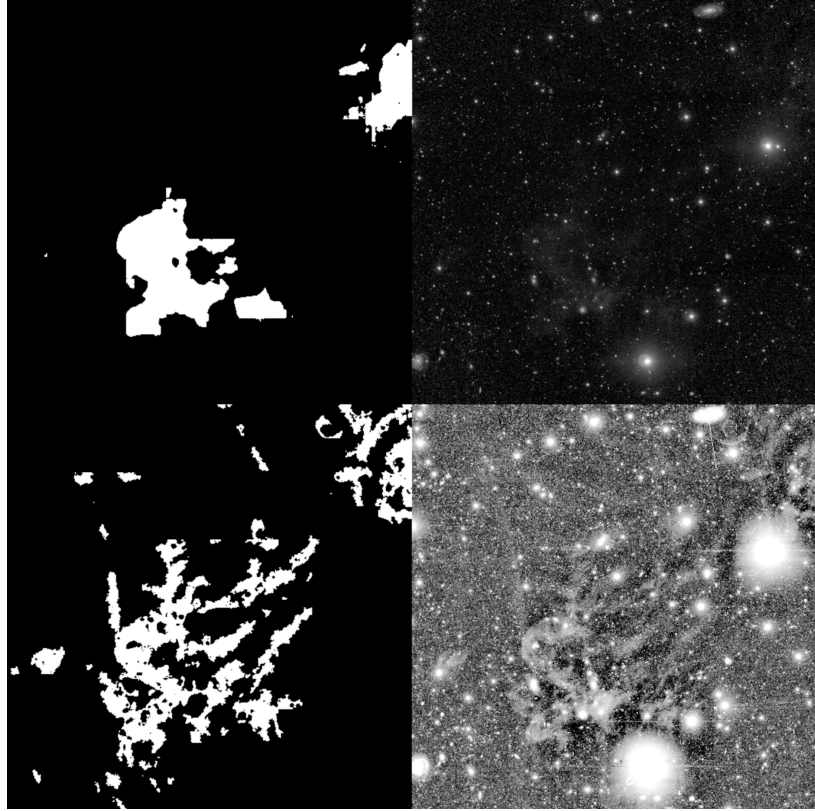


Figure 7: Cirrus maps and images in the r band for the f1082 field. The top row contains the cirrus map on the left and the image from the SDSS Stripe 82 on the right. The bottom row contains the cirrus map on the left and the image from the HSC-SSP on the right.

$\alpha \sim -1.5^h$ and $\delta \sim 1^\circ$. We should note that while this cloud does appear to be a large, coherent structure, it was not the case in Román et al. (2020) and Smirnov et al. (2023), where only Stripe 82 data was used. In Román et al. (2020), this cloud was divided into several smaller parts (see Fields 2-3 and Fields 6-10 in Table 2 of that work). Since Stripe 82 data is limited by $\delta = \pm 1.25^\circ$, the extension of this cloud toward higher declination values was not previously studied in deep optical images. Our study demonstrates that this is now possible using HSC-SSP data. In contrast, the left part of the Intersection region is almost devoid of cirrus, though a thin filamentary structure is still present. In the Spring region, a similar pattern is observed: the right part of the region contains numerous cirrus filaments, while the left part is nearly devoid of them. Also, note that the cirrus in this region appears as a collection of inclined stripes, revealing the characteristic filamentary structure of cirrus across multiple stacked HSC-SSP fields. We highlight that this is the first study of the global structure of cirrus clouds in this region of the sky using deep optical imaging, as Stripe 82 does not cover this area at all. In contrast, the North region is less noteworthy, as it contains almost no cirrus. We identified only a few small cirrus patches, with no clear evidence of a larger-scale dust structure.

In each subplot, we also provide contours for Galactic latitude. As seen in the data, most of the identified cirrus clouds are located between $b = 30^\circ$ and $b = 60^\circ$, as well as $b = -60^\circ$ and $b = -40^\circ$.

4.3. Cirrus properties

In this section, we analyze how bright the cirrus is compared to background noise and how cirrus fluxes in different bands correlate with each other. First, we assess how well the filaments stand out from the background noise. Fig. 10 shows the surface brightness of the filaments identified in the Spring region as a function of their size (total filament area). The surface brightness of a given filament is measured in the the manner as it is usually measured for extended objects: $\mu = -2.5 \log 10(F/S) + m_0$, where S is an area of a given filament, F is the total flux inside the filament's

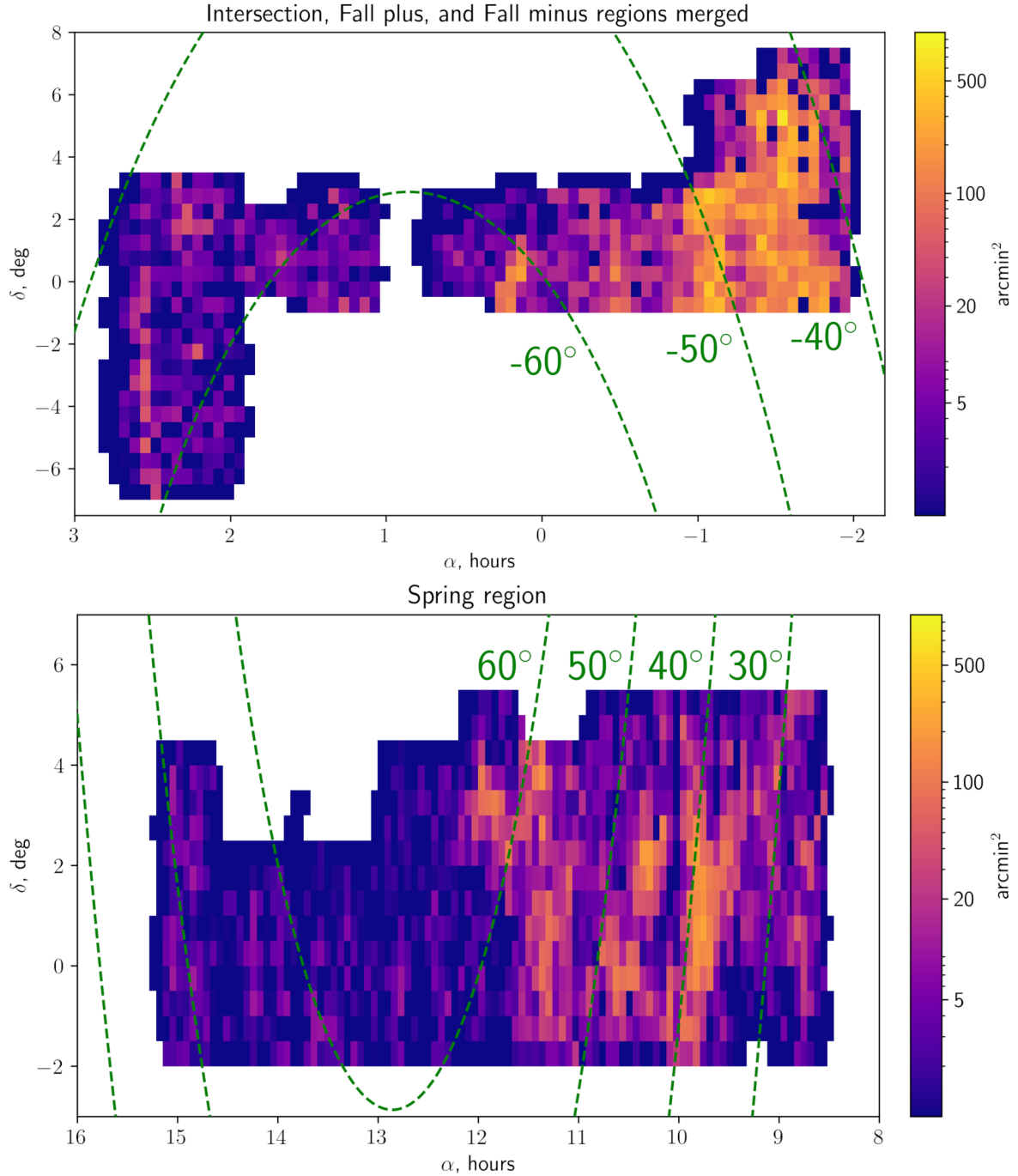


Figure 8: Cirrus maps obtained in the present work for the Intersection, Fall plus, Fall minus regions (top) and Spring region (bottom). Each rectangle in these maps corresponds to a bin of 1 deg in right ascension and 0.5 deg in declination. In each subplot, green lines indicate the Galactic latitude contours. The color of each bin corresponds to the total area covered by cirrus within a bin of 1 deg in right ascension and 0.5 deg in declination.

area, and $m_0 = 27$ mag is the photometric zero-point. We also plot the 3-sigma noise limit as a function of filament area. The exact value of the limit for different areas was determined using a sample of randomly placed squares which had a certain area value. After the sigma value was calculated for each square, it was averaged across all squares. As

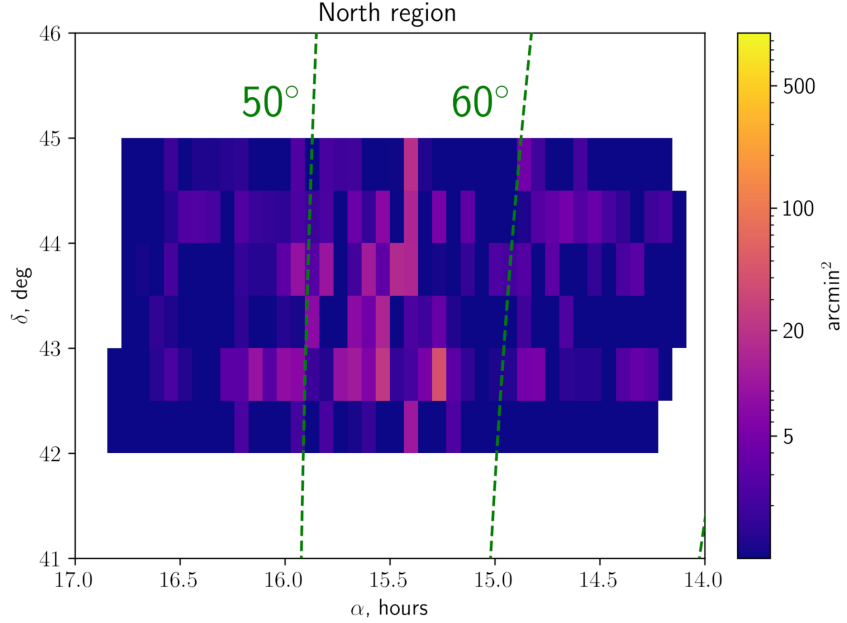


Figure 9: A cirrus map obtained in the present work for the North region. Each rectangle in this map corresponds to a bin of 1 deg in right ascension and 0.5 deg in declination. Green lines indicate the Galactic latitude contours. The color of each bin corresponds to the total area covered by cirrus within a bin of 1 deg in right ascension and 0.5 deg in declination.

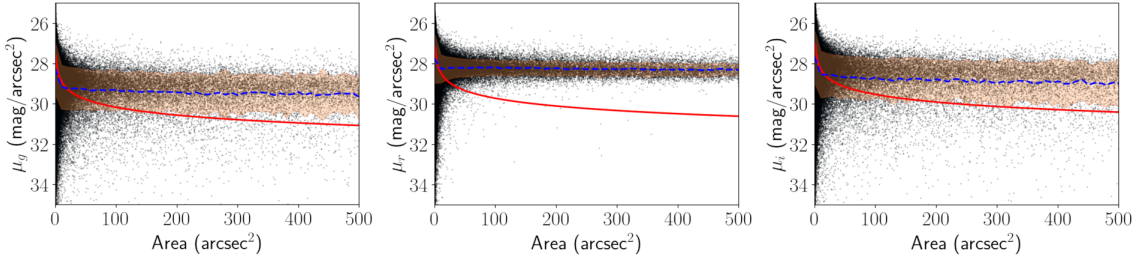


Figure 10: Surface brightness of filaments in the Spring region depending on the area in the g , r , and i optical bands (from left to right). A red line in each subplot marks the 3-sigma limit for the corresponding band. A blue dashed line shows the average value while the shaded area corresponds to 1-sigma limits.

can be seen, most filaments lie well above the limits, indicating that they are bright enough to be clearly distinguished from the background noise. However, we should also note that there is a tail of small filaments extending below the 3-sigma limits. This is naturally explained by the fact that the total flux in small filaments is more susceptible to disruptions from noise and over-subtraction by the background algorithm (see Section 5.2). Nevertheless, the neural network identifies these small filaments as cirrus based on their morphology, even though they cannot be distinguished from noise using the signal-to-noise ratio alone.

Secondly, compared to the g and i bands, the flux distribution in the r band is more concentrated above the 3-sigma limit across different area values. In the g and i bands, filaments more frequently appear below the 3-sigma limits. This difference between bands may be attributed to the fact that the training sample of filaments was prepared using only r -band images, while the cirrus mask remains unchanged for other optical bands. Although we focused on the Spring region in this discussion, the results are highly similar across other HSC-SSP regions. Fig. D.21 in Appendix D shows the plots for these regions.

Following our previous work (Smirnov et al., 2023), we calculated Pearson correlation coefficients between dif-

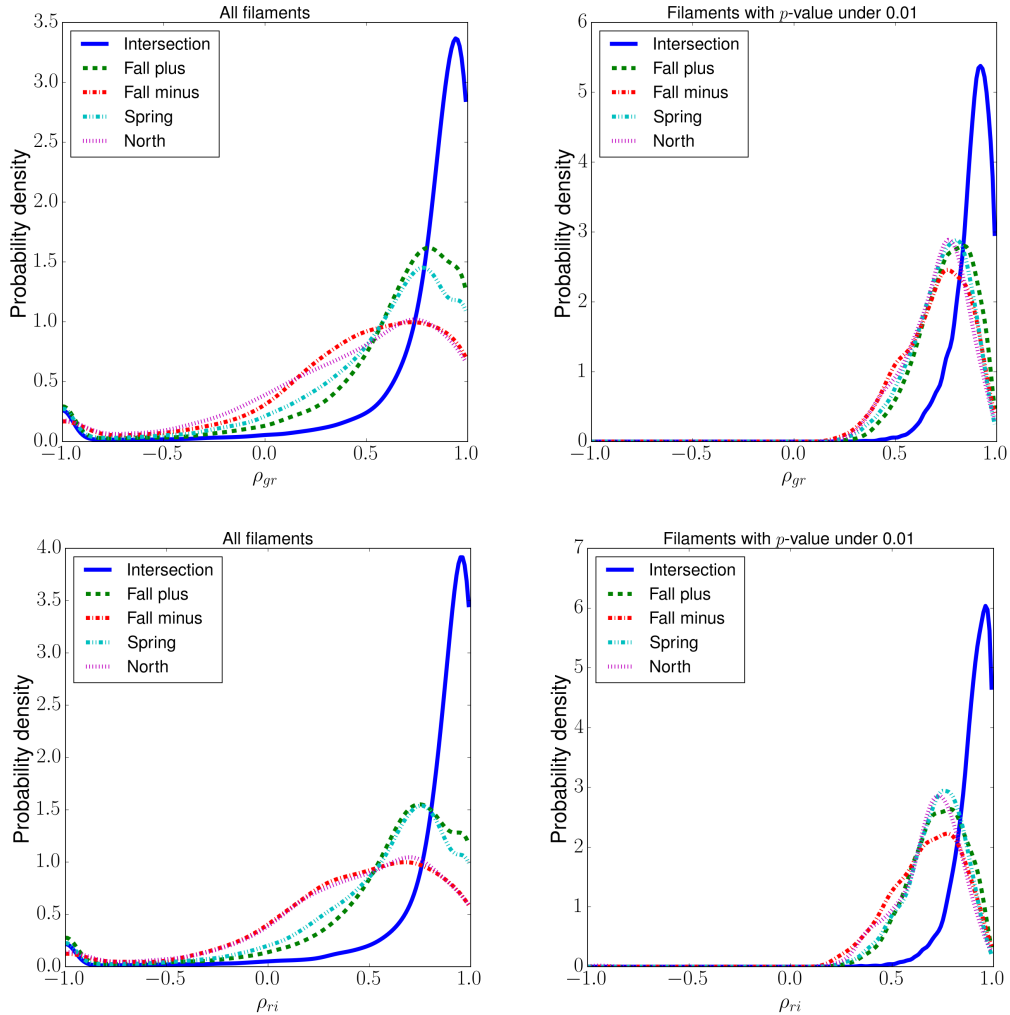


Figure 11: Distributions of Pearson correlation coefficients between different optical bands for cirrus filaments in HSC-SSP regions. Top row: g and r bands; Bottom row: r and i bands; Left column: for all filaments; Right column: only for statistically significant correlation with p -value under 0.01.

ferent optical bands for each filament:

$$\rho_{xy} = \frac{\sum_{i=1}^n (x_i - \bar{x})(y_i - \bar{y})}{\sqrt{\sum_{i=1}^n (x_i - \bar{x})^2} \sqrt{\sum_{i=1}^n (y_i - \bar{y})^2}}, \quad (1)$$

where x_i and y_i are the fluxes of the i -th pixel of the filament in x and y bands, respectively, and \bar{x} and \bar{y} are the mean fluxes found by averaging over all pixels contained in the filament area. It is worth noting that a combined mask was applied to the cirrus map before the correlation coefficients were calculated. To estimate the correlations, we also rebinned the data (the original g , r , and i images, as well as the cirrus maps and combined masks) to a 6-arcsecond resolution. This also facilitates direct comparison with the results of Smirnov et al. (2023), which were obtained at this exact spatial resolution.

Fig. 11 presents the distributions of correlation coefficients for all filaments and for those with a statistically significant correlation (p -value < 0.01). For these calculations we used `pearsonr` function from `scipy`. It is worth noting that this test requires a normality test, but we did not perform it. For some filaments, this condition may not be met, but we prefer to filter out filaments with a certain degree of error rather than not filtering them at all. As shown in the figure, the correlation coefficients exhibit a wide distribution, with some filaments even displaying negative correlations. Such cases arise when a filament contains a small number of pixels, making its total flux highly susceptible to disruptions from noise or other sources of error, such as proximity to bright sources, background subtraction issues, or flat-fielding artifacts. We effectively excluded these filaments from further analysis by filtering them based on the p -value of their correlation: p -value < 0.01 . As can be seen, applying this criterion shows that most filaments with statistically significant correlation exhibit positive correlation coefficients: $\rho_{gr} > 0.5$ and $\rho_{ri} > 0.5$. A significant correlation is generally expected for any source; however, since all compact sources have been masked, the observed correlation is likely associated with either cirrus filaments or other components of diffuse Galactic light. Thus, Fig. 11 demonstrates that our cirrus identification methods successfully detect well-correlated cirrus filaments at a spatial scale of 6 arcsec.

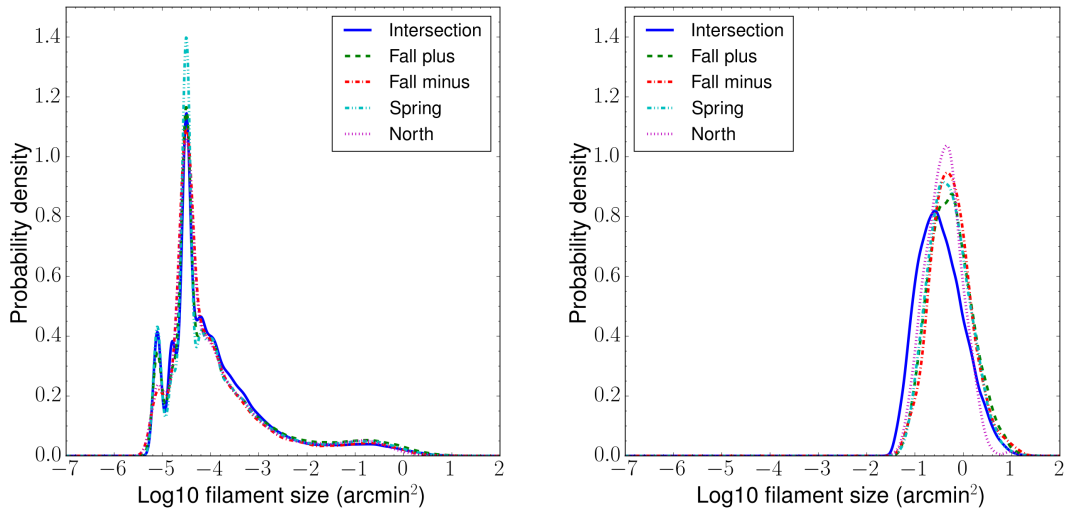


Figure 12: Distribution of sizes of individual filaments in HSC-SSP regions for the original resolution of HSC-SSP 0.168 arcsec (*left*) and for the data rebinned to the resolution of 6 arcsec (*right*).

Fig. 12 presents the size distribution of filaments at two different resolutions: the original HSC-SSP resolution of 0.168 arcsec and the 6-arcsecond resolution, considering only filaments with a statistically significant correlation (p -value < 0.01). As before, a combined mask was applied to the cirrus map before calculating the size distribution of filaments. It is also worth noting that filaments touching along the boundaries of fields are considered to be separate filaments, as in Smirnov et al. (2023). We present the size distribution at two different resolutions because

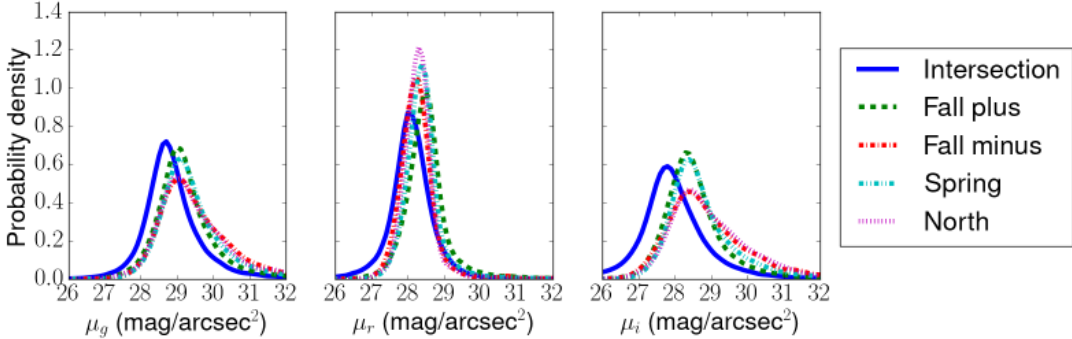


Figure 13: Distributions of the surface brightnesses of individual filaments in the HSC-SSP regions, in g , r , and i bands (from left to right, respectively), for data rebinned to a resolution of 6 arcsec.

examining both cases provides valuable insights into how filament properties change with spatial scale. For the original resolution, we see that the sample is dominated by very small filaments with a typical size of about 3–4 pixels (0.5–0.6 arcsec). A small peak to the left corresponds to the area of a single HSC-SSP pixel ($\approx 0.03 \text{ arcsec}^2$). At the same time, large filaments (\sim several arcmin 2) — comparable in size to some galaxies — are present across all HSC-SSP regions.

At the 6-arcsecond resolution (right panel of Fig. 12), the size distributions appear noticeably different. First, since the smallest scale is now 6 arcsec, all filaments smaller than this threshold are effectively filtered out. Secondly, applying the p -value filter causes the distribution peaks to shift to a characteristic value higher than the smallest allowed scale of 6 arcsec. This value varies slightly across individual regions but remains approximately 0.5–1.0 arcmin 2 for all HSC-SSP regions. This is in good agreement with the findings of Smirnov et al. (2023) for 6-arcsecond resolution, where the typical filament size in Stripe 82 data was found to be approximately 1 arcmin 2 . It is also important to note that, although the size distributions at the original resolution and 6-arcsecond resolution appear quite different, the total area covered by cirrus remains nearly the same in both cases: 13.3 deg 2 at the original resolution and 12.6 deg 2 for filaments with statistically significant correlation at 6-arcsecond resolution. This is because the majority of identified cirrus is contained within large, extended filaments, rather than in small patches with sizes below 6 arcseconds.

Taking into account that only filaments filtered by p -value have a strong correlation between fluxes in optical bands, we prepared two versions of cirrus filament catalogs for the entire HSC-SSP. The first catalog contains all the detected cirrus filaments that remain after rebinning to a 6-arcsecond resolution. Therefore, all filaments with an area greater than 36 arcsec 2 are contained in this catalog. The second catalog consists of filaments filtered by the p -value from the first one. Both catalogs are available on our GitLab repository⁵. Fig. 13 presents the distributions of surface brightnesses of individual filaments in the g , r , and i bands. These distributions are qualitatively similar across different HSC-SSP regions, with filaments in the Intersection region exhibiting the highest average brightness.

While the colors of filaments are important properties of cirrus, we intentionally do not analyze their distributions here. This is because cirrus fluxes in HSC-SSP data may be affected by background subtraction, potentially leading to incorrect estimations. We discuss this issue in detail in Section 5.

5. Discussion

5.1. Comparison of HSC-SSP data with Stripe 82 data

Fig. 14 compares the probability density distribution of the surface brightness of cirrus filaments identified in Smirnov et al. (2023) from Stripe 82 data at a resolution of 6 arcsec with those found in the Intersection region in this

⁵https://gitlab.com/polyakovdmi93/cirrus_narrow_segmentation

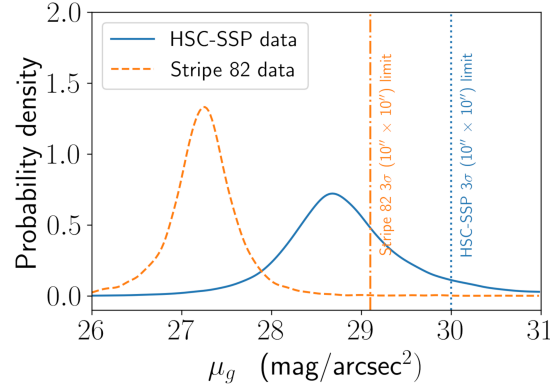


Figure 14: Comparison of g -band surface brightnesses distributions for individual filaments in the Intersection region for Stripe 82 from Smirnov et al. (2023) and HSC-SSP data (this work). Vertical lines indicate the $3\sigma(10'' \times 10'')$ surface brightness limits in the g band for the corresponding surveys.

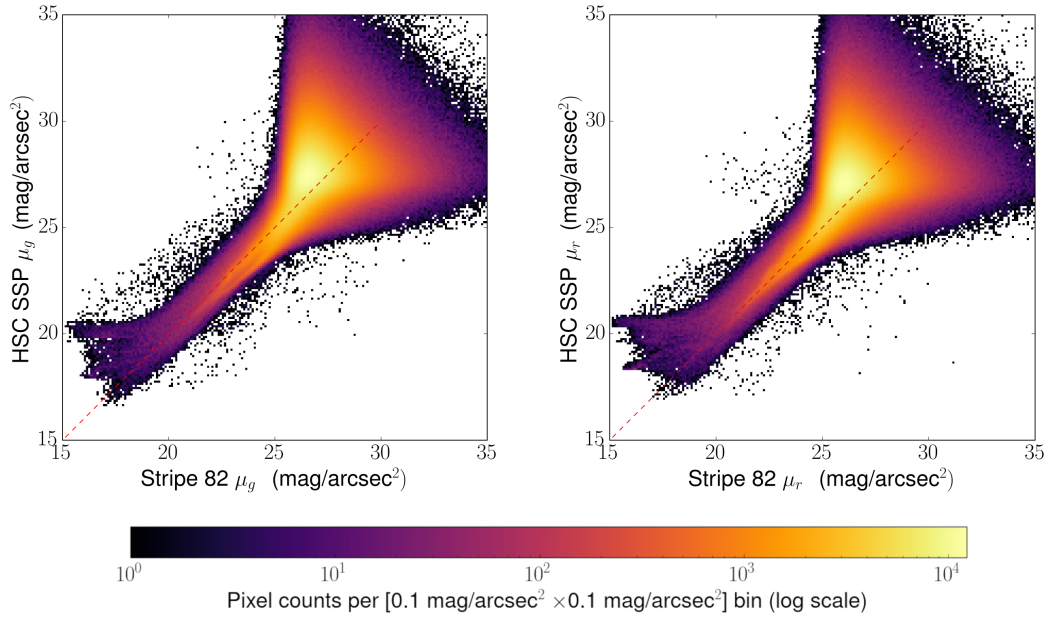


Figure 15: Pixel by pixel comparison of surface brightnesses in Stripe 82 and HSC-SSP data for the Field f1053 in the g (left) and r (right) optical bands.

study (at the same 6-arcsecond resolution). It is important to note that HSC-SSP covers only a portion of the original Stripe 82 data; therefore, we consider only the common fields from both datasets in this analysis. In Fig. 14, we expected the distributions to resemble each other. However, this is clearly not the case. The distributions are shifted relative to one another, indicating that the filaments in HSC-SSP appear dimmer, with the distribution mode shifted by approximately $\Delta\mu_g \sim 2 \text{ mag arcsec}^{-2}$. Also, the distribution from the original Stripe 82 data is slightly sharper and narrower.

To identify the root of the discrepancy, we performed a pixel-by-pixel comparison in the g and r bands for selected fields in Stripe 82 and HSC-SSP data. Fig. 15 shows this comparison for Field f1053, which is very rich in cirrus. Since HSC-SSP and Stripe 82 data have different native resolutions, we rebinned the HSC-SSP image to match the SDSS resolution of 0.396 arcsec/pixel. Note that the comparison includes all pixels from the original fields. In other words, no masking was done, and no cirrus was selected when we carried out this comparison. This is done so to demonstrate that, for bright sources, the fluxes are nearly the same. The figure indeed shows a strong 1:1 correlation up to a certain surface brightness level in both bands. However, beyond approximately 26–27 mag arcsec $^{-2}$, this correlation is no more. HSC SSP flux values are on average smaller (magnitudes are larger) and there is a large spread of values from the 1:1 line. Figs. 14 and 15 suggest that cirrus in the HSC-SSP data may be affected by background over-subtraction. We examine this issue in detail in the next section.

5.2. Over-subtraction areas in HSC-SSP

In the previous section, we demonstrated that cirrus in HSC-SSP data may be affected by background over-subtraction. To assess its impact, we examined the properties of various layers adjacent to cirrus filaments.

The boundary layer $L_{d,t}$ in a field is defined by the distance d from the cirrus and its thickness t . We calculate this layer using mathematical morphology applied to field's cirrus maps, as described below.

$$L_{d,t} = \begin{cases} (F \oplus K_{\text{out}}) \setminus (F \oplus K_{\text{in}}) \setminus M_c, & d > 0 \\ (F \oplus K_{\text{out}}) \setminus F \setminus M_c, & d \equiv 0 \end{cases}, \quad (2)$$

where F is the field cirrus map, \oplus denotes a dilation operation, \setminus denotes a set difference operation, M_c is a combined mask. We use the combined mask to exclude non-cirrus sources from analysis. K_{out} and K_{in} are circle structuring elements defined using the OpenCV library.

```
k_out = cv2.getStructuringElement(cv2.MORPH_ELLIPSE, (2 * (t + d) + 1, 2 * (t + d) + 1))
k_in = cv2.getStructuringElement(cv2.MORPH_ELLIPSE, (2 * d + 1, 2 * d + 1))
```

The properties of boundary layers were analyzed for fields in the Intersection region. As an example, Fig. 16 illustrates the boundary layer for Field f1053.

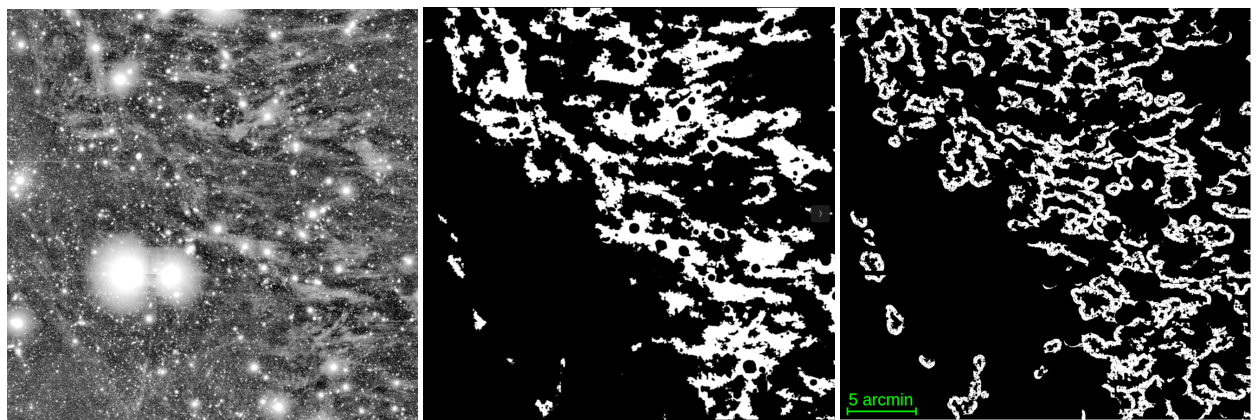


Figure 16: Example of boundary layer $L_{0,100}$ for field f1053. The field itself in the r band is shown in the left panel. The central panel shows the ensemble-generated cirrus map. The boundary layer is demonstrated in the right panel.

The simplest way to estimate the characteristic value of over-subtraction in a boundary layer is to compare the median pixel value within the layer to the median value in the background. Alternatively, for fields with a significant presence of cirrus filaments, one can compare the corresponding fractions of negative pixels. To start, we considered the boundary layer with a thickness of 100 pixels adjacent to cirrus, denoted as $L_{0,100}$, in fields where the cirrus fraction exceeds 0.1. There are 98 such fields in the Intersection region. For each field in the r band, we calculated the median pixel value of $L_{0,100}$, denoted as $m(L_{0,100})$. For the same fields, we also computed the fraction of negative pixels, $f_{-0}(L_{0,100})$. Next, we calculated the median values of $m(L_{0,100})$ and $f_{-0}(L_{0,100})$: $\langle m(L_{0,100}) \rangle = -1.49 \times 10^{-3}$, $\langle f_{-0}(L_{0,100}) \rangle = 0.512$. Then, we computed similar values for the background⁶ pixels in the same fields. Also note that some cirrus and boundary layer pixels are inevitably included in B . The median values for the background are $\langle m(B) \rangle = 4.67 \times 10^{-4}$ and $\langle f_{-0}(B) \rangle = 0.496$. Thus, the median value in pixels of the boundary layer is less than the corresponding value in the background, then this indicates an over-subtraction of background in the boundary layer. To demonstrate the statistical significance of this conclusion, we performed a Wilcoxon signed-rank test with a “less” alternative for the pairs of samples $(m(L_{0,100}), m(B))$ and $(f_{-0}(B), f_{-0}(L_{0,100}))$. These tests yielded p -values of 4.9×10^{-18} and 4.7×10^{-18} , respectively. Therefore, the null hypotheses can be reliably rejected.

Next, we examined the relationship between the fraction of cirrus in a field and the degree of over-subtraction in the boundary layer, represented by $m(L_{d,t})$. For the 98 previously analyzed fields, we calculated the median pixel value in the g , r and i bands for boundary layers with a thickness of 100 pixels: $L_{0,100}$, $L_{50,100}$, $L_{100,100}$, $L_{150,100}$, $L_{200,100}$. The scatter plots of these values are presented in the top panel of Fig. 17. The corresponding second-degree polynomial approximations are shown in the bottom panel. As evident from these graphs, the regions experiencing the most significant over-subtraction are concentrated approximately 100–200 pixels away from cirrus filaments in each band. Additionally, it is noteworthy that a higher cirrus fraction anti correlates with an increase in $m(L_{d,t})$ across all analyzed layers. To further illustrate the presence of an over-subtracted region near cirrus filaments, we analyzed the median values in layers $L_{x,100}$ for six cirrus-rich fields: f1053, f1052, f1043, f0453, f0495, and f1044. The cirrus fraction decreases from 0.209 in f1053 to 0.161 in f1044. These median values are presented in Fig. 18. For comparison, a horizontal reference line is included in the graph, representing the average of the median background values (excluding cirrus and the layer $L_{0,500}$) across the six selected fields. The graphs indicate that the most over-subtracted layers are those located 50–150 pixels away from cirrus filaments in these fields.

Thus, the magnitude of the over-subtraction depends on both the cirrus fraction and its distance, and we assume it is also influenced by the intrinsic properties of the cirrus itself. To evaluate the impact of over-subtraction, we estimate how much the surface brightness of a source would change, assuming that the over-subtraction is uniform and equal to the median of pixel value calculated for the 98 fields discussed above for the various $L_{x,100}$ layers. This effect is demonstrated in Fig. 19 in the g , r and i bands. As evident from the graph for the r band, even when assessing over-subtraction using the lowest median values of $m(L_{0,100})$, it results in a surface brightness bias of 0.5 magnitudes for objects with a surface brightness of $m = 29$ mag arcsec $^{-2}$ in the r band. It is worth mentioned that medians of pixel value in g and i bands are sufficiently larger than for the r band. This difference may be attributed to the circumstance that the cirrus maps are more precisely matched to the cirrus filaments in the r band because the training sample of the filaments was prepared using only r -band images. Although these estimates are approximate, it is evident that large cirrus filaments significantly impact the accuracy of sky background subtraction. Therefore, their presence should be taken into account in algorithms for sky background estimation. The cirrus maps we have generated can aid in refining these techniques for both existing and upcoming deep optical surveys, such as Euclid (Laureijs et al., 2011) or the Vera C. Rubin Observatory (former LSST, LSST Science Collaboration et al., 2009).

Unfortunately, sky background over-subtraction can also affect the visible boundaries of cirrus filaments, which can affect the reliability of cirrus maps. It is difficult to determine how much this influence is, as well as the value of sky background over-subtraction. However, the background of the sky in the HSC-SSP DR3 is taken into account on a large scale for “global-sky” coadd images (8K \times 8K superpixels was used to estimate it). Therefore, the value of sky background over-subtraction also varies on a large scale. If this scale exceeds the flux change scale at the boundaries of filaments, sky over-subtraction does not significantly affect the location of the visible boundaries of cirrus clouds.

An indirect way to verify the reliability of finding the boundaries of cirrus filaments is to compare them with data from other surveys. However, it is worth noting that the surface brightness limit of survey images is very important

⁶The background is defined as the area where the combined mask is 0: $B \equiv \overline{M_c}$

for determining the visible position of filament boundaries, as well as for the boundaries of galaxies. The difference in the cirrus fraction in the Intersection region obtained from HSC-SSP DR3 and SDSS Stripe 82 ($f_{\text{HSC-SSP}} = 0.0408$, $f_{\text{S82}} = 0.0092$) confirms the importance of the surface brightness limit of images. Thus, the best comparison would be with a survey of the same surface brightness limit.

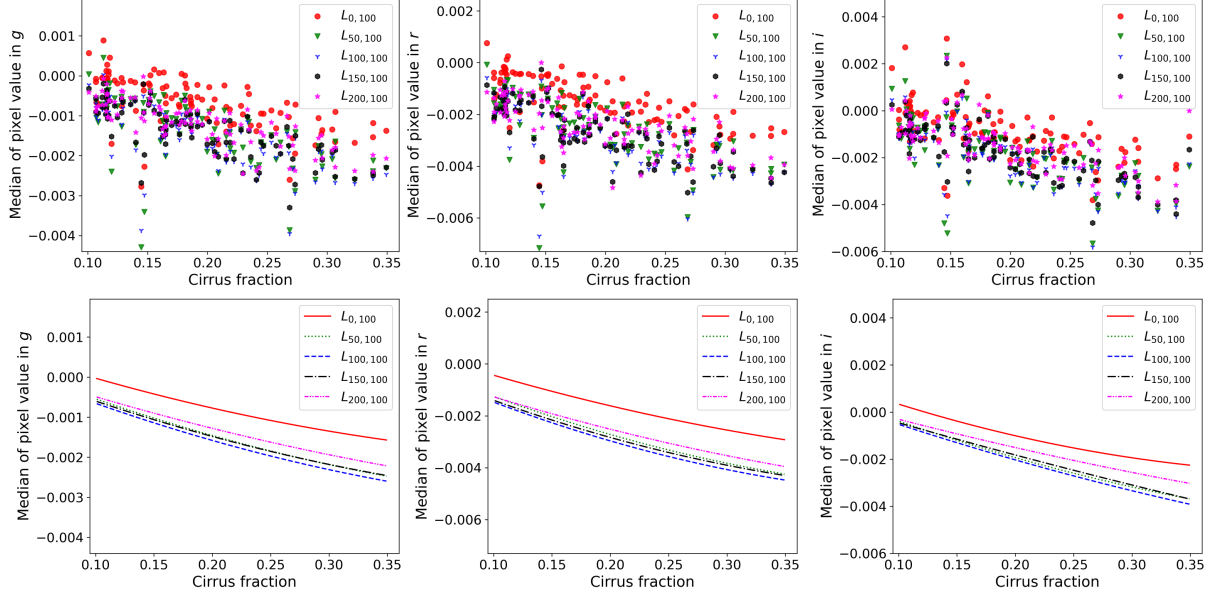


Figure 17: The top panel contains scatter plots of the median values in the boundary layers with a thickness of 100 pixels ($L_{0,100}$, $L_{50,100}$, $L_{100,100}$, $L_{150,100}$, $L_{200,100}$) in the g , r and i optical bands (from left to right) for fields in the Intersection region, where the fraction of cirrus is greater than 0.1. The bottom panel contains corresponding approximations by polynomials of the second degree.

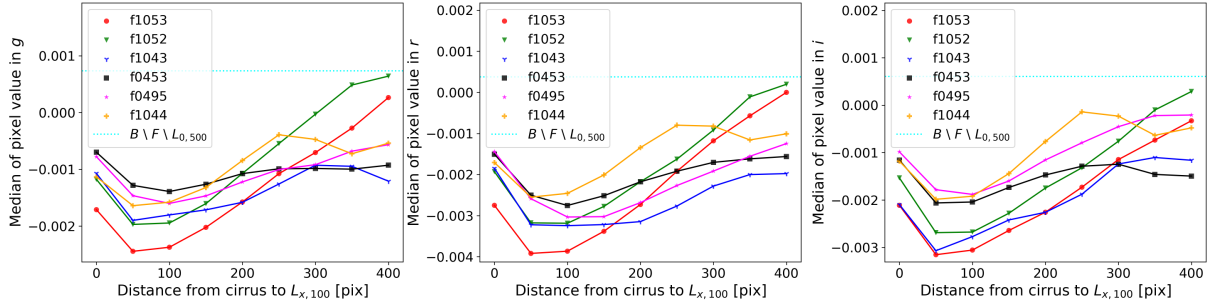


Figure 18: Median values in the boundary layers $L_{x,100}$ in the g , r and i optical bands (from left to right) for six fields f1053, f1052, f1043, f0453, f0495, and f1044 are represented by different colored dots. The horizontal dotted line denotes the average of median values of the background without the cirrus and the layer $L_{0,500}$ for the six fields considered.

6. Summary and conclusions

In this study, we have analyzed cirri in the HSC-SSP DR3 data as a continuation of Smirnov et al. (2023), which investigated the color properties of cirrus using Stripe 82 data. In Smirnov et al. (2023), a catalog of cirrus filaments was created using a neural network trained on a dataset of semi-automatically generated cirrus maps, with the best model achieving an IoU of 0.576 for cirrus. Here, we adopted a similar neural network architecture to identify cirrus filaments in the new HSC-SSP data.

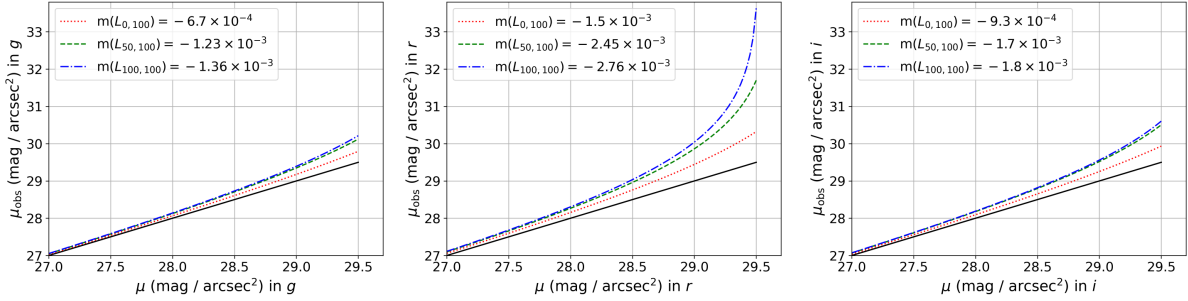


Figure 19: Bias in the observed surface brightness of the source due to over-subtraction of various values in the g , r and i optical bands (from left to right). The bias values correspond to the medians of the pixel value for different boundary layers: $L_{0,100}$, $L_{50,100}$ and $L_{100,100}$. The ground-truth surface brightness of the source is plotted along the x-axis. Biased observed surface brightness is plotted along the y-axis. Solid lines correspond to the 1:1 line.

Since individual models exhibited a lower IoU for cirrus than in Smirnov et al. (2023) ($\text{IoU} \leq 0.436$), we employed an ensemble of the nine best 4-channel models to generate the cirrus maps and catalog. Using this ensemble improved the IoU to 0.48. After compiling the catalog of cirrus filaments based on the HSC-SSP data, we compared our results with those from Smirnov et al. (2023). For 613 fields in the Intersection region, we obtained cirrus maps from both the Stripe 82 and HSC-SSP datasets. These maps demonstrate high consistency, despite the deeper HSC-SSP dataset revealing 4.5 times more cirrus clouds. The obtained cirrus maps for various regions of HSC-SSP are presented in Fig. 8 and Fig. 9. The cirrus filaments in the Spring, Fall plus, Fall minus, and North regions are studied for the first time in the present work. For all regions, the typical size of identified filaments is about 0.5–1.0 arcmin. The value is in agreement with the results of our previous work, where only Stripe 82 data was considered (Smirnov et al., 2023). The total area of identified cirri, summed across all the HSC-SSP regions analyzed, is approximately 13 deg^2 .

The cirrus filament catalogs and the rectified cirrus maps that we have created are publicly available in our GitLab repository⁷.

Through several tests, we revealed a discrepancy in the surface brightness of filaments between Stripe 82 and HSC-SSP data. This suggests that the background subtraction procedure in HSC-SSP results in the over-subtraction of cirrus fluxes, and possibly other faint sources. Using our cirrus maps, we examined the surface brightness in regions adjacent to the filaments and provided a rough estimate of the over-subtraction effect.

This study has validated the cirrus map creation approach proposed in Smirnov et al. (2023) and enhanced it through ensemble learning. We confirm the importance of accounting for cirrus in background estimation algorithms. Moving forward, we plan to refine our method for generating cirrus maps and extend its application to upcoming deep optical surveys.

Acknowledgements

We thank the anonymous referees by their detailed revision of the manuscript that helped to improve its quality.

We acknowledge financial support from the Russian Science Foundation (grant no. 20-72-10052).

The Hyper Suprime-Cam (HSC) collaboration includes the astronomical communities of Japan and Taiwan, and Princeton University. The HSC instrumentation and software were developed by the National Astronomical Observatory of Japan (NAOJ), the Kavli Institute for the Physics and Mathematics of the Universe (Kavli IPMU), the University of Tokyo, the High Energy Accelerator Research Organization (KEK), the Academia Sinica Institute for Astronomy and Astrophysics in Taiwan (ASIAA), and Princeton University. Funding was contributed by the FIRST program from the Japanese Cabinet Office, the Ministry of Education, Culture, Sports, Science and Technology (MEXT), the Japan Society for the Promotion of Science (JSPS), the Japan Science and Technology Agency (JST), the Toray Science Foundation, NAOJ, Kavli IPMU, KEK, ASIAA, and Princeton University. This paper makes use of software developed for the Large Synoptic Survey Telescope. We thank the LSST Project for making their code available as

⁷https://gitlab.com/polyakovdmi93/cirrus_narrow_segmentation

free software at <http://dm.lsst.org>. The Pan-STARRS1 Surveys have been made possible through contributions of the Institute for Astronomy, the University of Hawaii, the Pan-STARRS Project Office, the Max-Planck Society and its participating institutes, the Max Planck Institute for Astronomy, Heidelberg and the Max Planck Institute for Extraterrestrial Physics, Garching, The Johns Hopkins University, Durham University, the University of Edinburgh, Queen's University Belfast, the Harvard-Smithsonian Center for Astrophysics, the Las Cumbres Observatory Global Telescope Network Incorporated, the National Central University of Taiwan, the Space Telescope Science Institute, the National Aeronautics and Space Administration under Grant No. NNX08AR22G issued through the Planetary Science Division of the NASA Science Mission Directorate, the National Science Foundation under Grant No. AST-1238877, the University of Maryland, Eotvos Lorand University (ELTE), and the Los Alamos National Laboratory. This paper is based on data collected at the Subaru Telescope and retrieved from the HSC data archive system, which is operated by the Subaru Telescope and Astronomy Data Center at NAOJ.

Appendix A. Surface brightness limits of HSC-SSP

There, the process of obtaining surface brightness limits of HSC-SSP coadd images is described. In this paper, we define this value in the same way as Román et al. (2020) did. The surface brightness limit at 3σ level for a source with an angular size of $10'' \times 10''$ can be defined as follows:

$$\mu_{\text{lim}}(3\sigma; 10'' \times 10'') = m_0 - 2.5 \lg(3\sigma),$$

where σ is the standard deviation of the background flux in a random box with an angular size of $10'' \times 10''$, and m_0 is the photometric zero-point of the data in the optical band under consideration. The coadd images have a common photometric zero-point of 27.0 in all bands in the HSC-SSP.

To compute $\mu_{\text{lim}}(3\sigma; 10'' \times 10'')$ we directly estimate σ . For this procedure, we use all fields that we consider (4331 fields). For each field, we place 10000 random boxes with a size of $10'' \times 10''$, which do not intersect with the combined mask. Then, for each box, we calculate the standard deviation of the flux. This value is recalculated into stellar magnitudes using the photometric zero-point m_0 . Averaging this value over all 10000 boxes gives the surface brightness limit for the field. Then, averaging this value for all 4331 fields, we obtain the surface brightness limit for the HSC-SSP in the optical band under consideration.

Appendix B. Validation loss curves across 100 training epochs

One of the main stages of this work is training artificial neural networks to create cirrus maps. Finding optimal parameters for the network architecture and learning process requires repeatedly training various models. Since our computing resources were limited to a single NVIDIA GeForce RTX 3060 GPU graphics card, we needed to speed up the learning process of our models.

The simplest way, without affecting the network architecture or optimization process, is to reduce the number of training epochs. To make sure that reducing the number of training epochs does not significantly affect the final result, we trained 12 4-channel models. There are presented validation loss curves for these models across 100 training epochs. As can be clearly seen from Fig. B.20, the loss curves reach a plateau by the 20th epoch. This allows us to train models for 20 epochs in order to save time.

Appendix C. Metrics and parameters of cirrus segmentation models

Section 3.3 discusses the results of experiments on training neural network models to create cirrus maps.

The main results of the network training are presented here in the form of tables. Each model in these tables is represented by three parameters of the learning process: class weights ($\bar{\omega}_c$), the spatial size of the input tensor (shape), the ratio of the window size to the spatial size of the input tensor (scale), the learning rate (r) and metrics on the test sample: intersection over union (IoU, Jaccard, 1901), precision and recall for cirrus class. IoU metric measures the extent of correspondence between the predicted and actual cirrus map.

The metrics presented in Tables C.4 and C.5 allow one to compare the quality of 3-channel and 4-channel models. Table C.6 shows the results of an experiment on fine-tuning the best models from Smirnov et al. (2023).

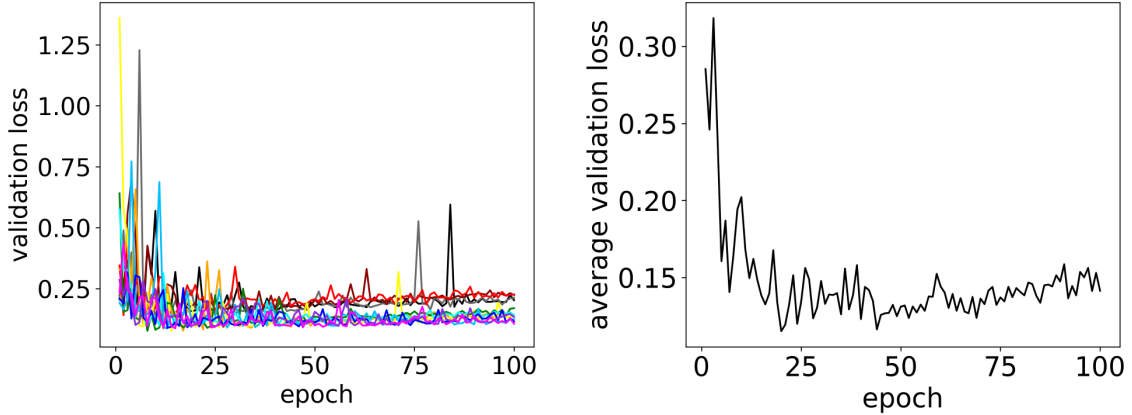


Figure B.20: The left panel shows validation loss curves across 100 epochs for 12 4-channel models. Validation loss curves of different colors correspond to different models. The corresponding average loss curve is presented in the right panel.

Table C.4: The results of the training experiments conducted on 3-channel models. It lists class weights for background and cirrus ($\bar{\omega}_c$), input tensor spatial shape, scale factor, learning rate (r) and IoU, precision, recall for all test fields for cirrus class.

$\bar{\omega}_c$	shape / scale	r	IoU	precision	recall
(1.0, 15.0)	448 × 448 / 2	0.0005	0.381	0.573	0.532
(1.0, 15.0)	448 × 448 / 2	0.0005	0.399	0.614	0.533
(1.0, 15.0)	448 × 448 / 2	0.001	0.344	0.607	0.442
(1.0, 15.0)	448 × 448 / 2	0.001	0.416	0.678	0.518
(1.0, 15.0)	448 × 448 / 4	0.0005	0.389	0.502	0.634
(1.0, 15.0)	448 × 448 / 4	0.0005	0.385	0.67	0.475
(1.0, 15.0)	448 × 448 / 4	0.001	0.355	0.537	0.512
(1.0, 15.0)	448 × 448 / 4	0.001	0.397	0.582	0.556
(1.0, 15.0)	448 × 448 / 8	0.0005	0.348	0.432	0.641
(1.0, 15.0)	448 × 448 / 8	0.0005	0.281	0.385	0.509
(1.0, 15.0)	448 × 448 / 8	0.001	0.298	0.536	0.402
(1.0, 15.0)	448 × 448 / 8	0.001	0.334	0.645	0.409

Table C.5: The results of the training experiments conducted on 4-channel models. It lists class weights for background and cirrus ($\bar{\omega}_c$), input tensor spatial shape, scale factor, learning rate (r) and IoU, precision, recall for all tests fields for cirrus class. The last column shows the rank of the model, if it is among the top 9 4-channel models based on the IoU metric.

$\bar{\omega}_c$	shape / scale	r	IoU	precision	recall	Rank among the top 9 models
(1.0, 10.0)	448 × 448 / 2	0.0005	0.317	0.641	0.385	
(1.0, 10.0)	448 × 448 / 2	0.0005	0.29	0.665	0.34	
(1.0, 10.0)	448 × 448 / 2	0.001	0.436	0.569	0.651	1
(1.0, 10.0)	448 × 448 / 2	0.001	0.322	0.791	0.352	
(1.0, 10.0)	448 × 448 / 4	0.0005	0.345	0.653	0.423	
(1.0, 10.0)	448 × 448 / 4	0.0005	0.395	0.634	0.511	
(1.0, 10.0)	448 × 448 / 4	0.001	0.362	0.555	0.51	
(1.0, 10.0)	448 × 448 / 4	0.001	0.424	0.672	0.535	2
(1.0, 10.0)	448 × 448 / 8	0.0005	0.379	0.543	0.556	
(1.0, 10.0)	448 × 448 / 8	0.0005	0.391	0.554	0.57	
(1.0, 10.0)	448 × 448 / 8	0.001	0.386	0.566	0.549	
(1.0, 10.0)	448 × 448 / 8	0.001	0.356	0.477	0.584	
(1.0, 10.0)	448 × 448 / 8	0.005	0.424	0.565	0.629	3
(1.0, 10.0)	448 × 448 / 8	0.005	0.373	0.547	0.54	
(1.0, 15.0)	448 × 448 / 2	0.0005	0.404	0.51	0.66	7
(1.0, 15.0)	448 × 448 / 2	0.0005	0.391	0.649	0.496	
(1.0, 15.0)	448 × 448 / 2	0.001	0.383	0.527	0.583	
(1.0, 15.0)	448 × 448 / 2	0.001	0.275	0.828	0.292	
(1.0, 15.0)	448 × 448 / 4	0.0005	0.375	0.574	0.519	
(1.0, 15.0)	448 × 448 / 4	0.0005	0.4	0.613	0.536	
(1.0, 15.0)	448 × 448 / 4	0.001	0.386	0.563	0.552	
(1.0, 15.0)	448 × 448 / 4	0.001	0.403	0.549	0.604	8
(1.0, 15.0)	448 × 448 / 8	0.0005	0.347	0.566	0.472	
(1.0, 15.0)	448 × 448 / 8	0.0005	0.304	0.511	0.429	
(1.0, 15.0)	448 × 448 / 8	0.001	0.35	0.679	0.42	
(1.0, 15.0)	448 × 448 / 8	0.001	0.338	0.547	0.47	
(1.0, 20.0)	448 × 448 / 2	0.0005	0.422	0.653	0.545	4
(1.0, 20.0)	448 × 448 / 2	0.0005	0.413	0.571	0.598	6
(1.0, 20.0)	448 × 448 / 2	0.001	0.394	0.527	0.609	
(1.0, 20.0)	448 × 448 / 2	0.001	0.337	0.421	0.627	
(1.0, 20.0)	448 × 448 / 4	0.0005	0.244	0.604	0.291	
(1.0, 20.0)	448 × 448 / 4	0.0005	0.375	0.504	0.593	
(1.0, 20.0)	448 × 448 / 4	0.001	0.312	0.53	0.431	
(1.0, 20.0)	448 × 448 / 4	0.001	0.33	0.613	0.417	
(1.0, 20.0)	448 × 448 / 8	0.0005	0.323	0.468	0.51	
(1.0, 20.0)	448 × 448 / 8	0.0005	0.401	0.504	0.666	9
(1.0, 20.0)	448 × 448 / 8	0.001	0.419	0.562	0.621	5
(1.0, 20.0)	448 × 448 / 8	0.001	0.363	0.479	0.601	

Table C.6: The results of fine-tuning the best model from Smirnov et al. (2023) using HSC-SSP data. It lists class weights for background and cirrus ($\bar{\omega}_c$), input tensor spatial shape, scale factor, learning rate (r) and IoU, precision, recall for all test fields for cirrus class.

$\bar{\omega}_c$	shape / scale	r	IoU	precision	recall
(1.0, 15.0)	448 × 448 / 2	0.0001	0.364	0.583	0.492
(1.0, 15.0)	448 × 448 / 2	0.0001	0.383	0.496	0.628
(1.0, 15.0)	448 × 448 / 2	0.00025	0.348	0.525	0.508
(1.0, 15.0)	448 × 448 / 2	0.00025	0.359	0.521	0.536
(1.0, 15.0)	448 × 448 / 2	0.0005	0.377	0.589	0.512
(1.0, 15.0)	448 × 448 / 2	0.0005	0.388	0.67	0.48
(1.0, 15.0)	448 × 448 / 2	0.001	0.338	0.56	0.46
(1.0, 15.0)	448 × 448 / 2	0.001	0.372	0.437	0.716
(1.0, 15.0)	448 × 448 / 3	0.0001	0.342	0.564	0.465
(1.0, 15.0)	448 × 448 / 3	0.0001	0.349	0.539	0.498
(1.0, 15.0)	448 × 448 / 3	0.00025	0.325	0.487	0.495
(1.0, 15.0)	448 × 448 / 3	0.00025	0.384	0.494	0.633
(1.0, 15.0)	448 × 448 / 3	0.0005	0.301	0.498	0.432
(1.0, 15.0)	448 × 448 / 3	0.0005	0.377	0.557	0.539
(1.0, 15.0)	448 × 448 / 3	0.001	0.287	0.582	0.362
(1.0, 15.0)	448 × 448 / 3	0.001	0.317	0.471	0.493

Appendix D. Surface brightness of filaments depending on the area

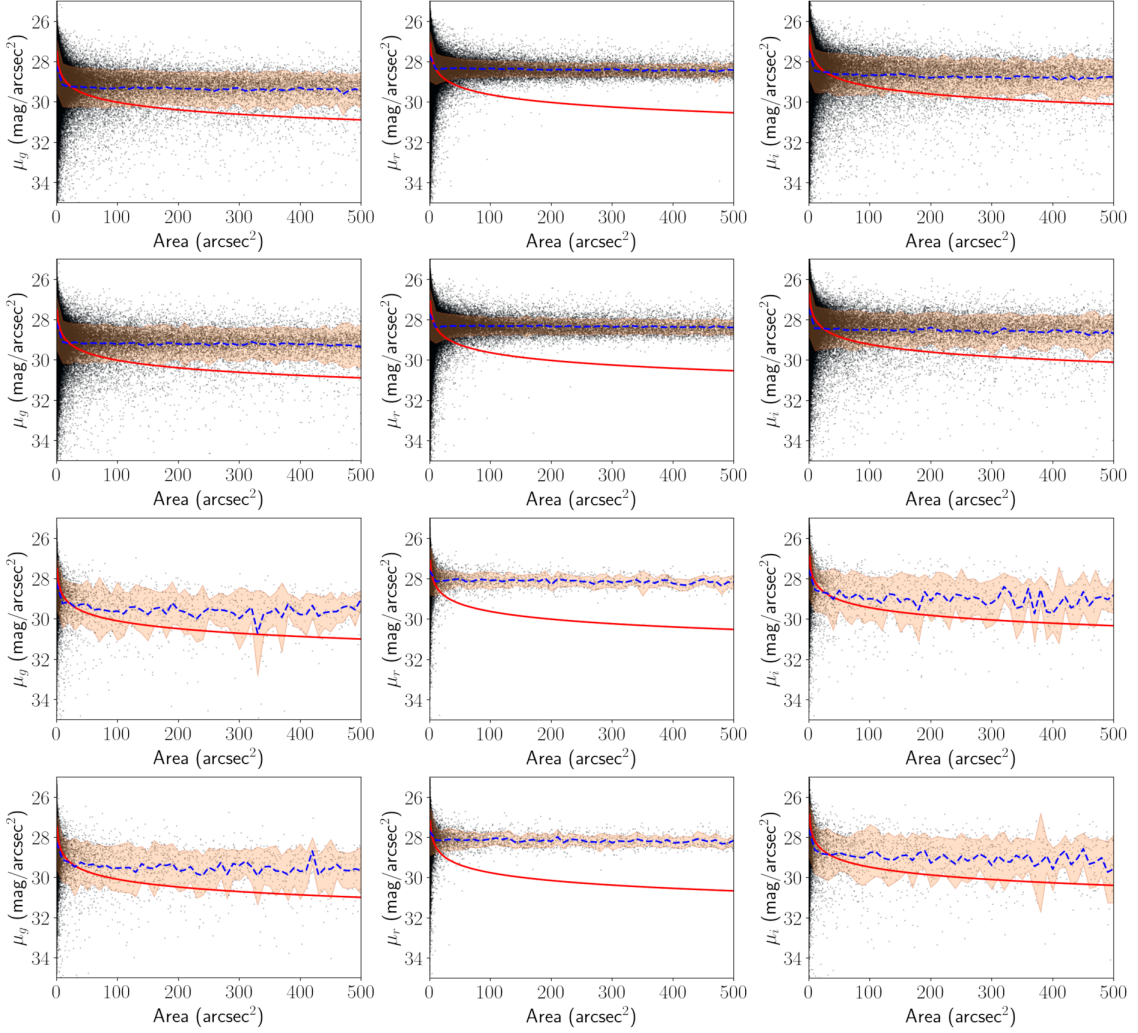


Figure D.21: Surface brightness of filaments in the Intersection, Fall plus, Fall minus, and North regions (from top to bottom) depending on the area in the g , r , and i optical bands (from left to right). A red line in each subplot marks the 3-sigma limit for the corresponding band. A blue dashed line shows the average value while the shaded area corresponds to 1-sigma limits.

References

Abazajian, K.N., Adelman-McCarthy, J.K., Agüeros, M.A., Allam, S.S., Allende Prieto, C., An, D., Anderson, K.S.J., Anderson, S.F., Annis, J., Bahcall, N.A., Bailer-Jones, C.A.L., Barentine, J.C., Bassett, B.A., Becker, A.C., Beers, T.C., Bell, E.F., Belokurov, V., Berlind, A.A., Berman, E.F., Bernardi, M., Bickerton, S.J., Bizyaev, D., Blakeslee, J.P., Blanton, M.R., Bochanski, J.J., Boroski, W.N., Brewington, H.J., Brinchmann, J., Brinkmann, J., Brunner, R.J., Budavári, T., Carey, L.N., Carliles, S., Carr, M.A., Castander, F.J., Cinabro, D., Connolly, A.J., Csabai, I., Cunha, C.E., Czarapata, P.C., Davenport, J.R.A., de Haas, E., Dilday, B., Doi, M., Eisenstein, D.J., Evans, M.L., Evans, N.W., Fan, X., Friedman, S.D., Frieman, J.A., Fukugita, M., Gänsicke, B.T., Gates, E., Gillespie, B., Gilmore, G., Gonzalez, B., Gonzalez, C.F., Grebel, E.K., Gunn, J.E., Györy, Z., Hall, P.B., Harding, P., Harris, F.H., Harvanek, M., Hawley, S.L., Hayes, J.J.E., Heckman, T.M., Hendry, J.S., Hennessy, G.S., Hindsley, R.B., Hoblitt, J., Hogan, C.J., Hogg, D.W., Holtzman, J.A., Hyde, J.B., Ichikawa, S.i., Ichikawa, T., Im, M., Ivezić, Ž., Jester, S., Jiang, L., Johnson, J.A., Jorgensen, A.M., Jurić, M., Kent, S.M., Kessler, R., Kleinman, S.J., Knapp, G.R., Konishi, K., Kron, R.G., Krzesinski, J., Kuropatkin, N., Lampeitl, H., Lebedeva, S., Lee, M.G., Lee, Y.S., French Leger, R., Lépine, S., Li, N., Lima, M., Lin, H., Long, D.C., Loomis, C.P., Loveday, J., Lupton, R.H., Magnier, E., Malanushenko, O., Malanushenko, V., Mandelbaum, R., Margon, B., Marriner, J.P., Martínez-Delgado, D., Matsubara, T., McGehee, P.M., McKay, T.A., Meiksin, A., Morrison, H.L., Mullally, F., Munn, J.A., Murphy, T., Nash, T., Nebot, A., Neilsen, Eric H., J., Newberg, H.J., Newman, P.R., Nichol, R.C., Nicinski, T., Nieto-Santisteban, M., Nitta, A., Okamura, S., Oravetz, D.J., Ostriker, J.P., Owen, R., Padmanabhan, N., Pan, K., Park, C., Pauls, G., Peoples, John, J., Percival, W.J., Pier, J.R., Pope, A.C., Pourbaix, D., Price, P.A., Purger, N., Quinn, T., Raddick, M.J., Re Fiorentin, P., Richards, G.T., Richmond, M.W., Riess, A.G., Rix, H.W., Rockosi, C.M., Sako, M., Schlegel, D.J., Schneider, D.P., Scholz, R.D., Schreiber, M.R., Schwope, A.D., Seljak, U., Sesar, B., Sheldon, E., Shimasaku, K., Sibley, V.C., Simmons, A.E., Sivarani, T., Allyn Smith, J., Smith, M.C., Smolčić, V., Snedden, S.A., Stebbins, A., Steinmetz, M., Stoughton, C., Strauss, M.A., SubbaRao, M., Suto, Y., Szalay, A.S., Szapudi, I., Szkody, P., Tanaka, M., Tegmark, M., Teodoro, L.F.A., Thakar, A.R., Tremonti, C.A., Tucker, D.L., Uomoto, A., Vanden Berk, D.E., Vandenberg, J., Vidrih, S., Vogeley, M.S., Voges, W., Vogt, N.P., Wadadekar, Y., Watters, S., Weinberg, D.H., West, A.A., White, S.D.M., Wilhite, B.C., Wonders, A.C., Yanny, B., Yocom, D.R., York, D.G., Zehavi, I., Zibetti, S., Zucker, D.B., 2009. The Seventh Data Release of the Sloan Digital Sky Survey. *ApJS* 182, 543–558. doi:10.1088/0067-0049/182/2/543, arXiv:0812.0649.

Aihara, H., AlSayyad, Y., Ando, M., Armstrong, R., Bosch, J., Egami, E., Furusawa, H., Furusawa, J., Goulding, A., Harikane, Y., Hikage, C., Ho, P.T.P., Hsieh, B.C., Huang, S., Ikeda, H., Imanishi, M., Ito, K., Iwata, I., Jaelani, A.T., Kakuma, R., Kawana, K., Kikuta, S., Kobayashi, U., Koike, M., Komiyama, Y., Li, X., Liang, Y., Lin, Y.T., Luo, W., Lupton, R., Lust, N.B., MacArthur, L.A., Matsuoka, Y., Mineo, S., Miyatake, H., Miyazaki, S., More, S., Murata, R., Namiki, S.V., Nishizawa, A.J., Oguri, M., Okabe, N., Okamoto, S., Okura, Y., Ono, Y., Onodera, M., Onoue, M., Osato, K., Ouchi, M., Shibuya, T., Strauss, M.A., Sugiyama, N., Suto, Y., Takada, M., Takagi, Y., Takata, T., Takita, S., Tanaka, M., Terai, T., Toba, Y., Uchiyama, H., Utsumi, Y., Wang, S.Y., Wang, W., Yamada, Y., 2019. Second data release of the Hyper Suprime-Cam Subaru Strategic Program. *PASJ* 71, 114. doi:10.1093/pasj/psz103, arXiv:1905.12221.

Aihara, H., AlSayyad, Y., Ando, M., Armstrong, R., Bosch, J., Egami, E., Furusawa, H., Furusawa, J., Harasawa, S., Harikane, Y., Hsieh, B.C., Ikeda, H., Ito, K., Iwata, I., Kodama, T., Koike, M., Kokubo, M., Komiyama, Y., Li, X., Liang, Y., Lin, Y.T., Lupton, R.H., Lust, N.B., MacArthur, L.A., Mawatari, K., Mineo, S., Miyatake, H., Miyazaki, S., More, S., Morishima, T., Murayama, H., Nakajima, K., Nakata, F., Nishizawa, A.J., Oguri, M., Okabe, N., Okura, Y., Ono, Y., Osato, K., Ouchi, M., Pan, Y.C., Plazas Malagón, A.A., Price, P.A., Reed, S.L., Rykoff, E.S., Shibuya, T., Simunovic, M., Strauss, M.A., Sugimori, K., Suto, Y., Suzuki, N., Takada, M., Takagi, Y., Takata, T., Takita, S., Tanaka, M., Tang, S., Tararu, D.S., Terai, T., Toba, Y., Turner, E.L., Uchiyama, H., Vijarnwannaluk, B., Waters, C.Z., Yamada, Y., Yamamoto, N., Yamashita, T., 2022. Third data release of the Hyper Suprime-Cam Subaru Strategic Program. *PASJ* 74, 247–272. doi:10.1093/pasj/psab122, arXiv:2108.13045.

Aihara, H., Armstrong, R., Bickerton, S., Bosch, J., Coupon, J., Furusawa, H., Hayashi, Y., Ikeda, H., Kamata, Y., Karoji, H., Kawanomoto, S., Koike, M., Komiyama, Y., Lang, D., Lupton, R.H., Mineo, S., Miyatake, H., Miyazaki, S., Morokuma, T., Obuchi, Y., Oishi, Y., Okura, Y., Price, P.A., Takata, T., Tanaka, M.M., Tanaka, M.,

Tanaka, Y., Uchida, T., Uraguchi, F., Utsumi, Y., Wang, S.Y., Yamada, Y., Yamanoi, H., Yasuda, N., Arimoto, N., Chiba, M., Finet, F., Fujimori, H., Fujimoto, S., Furusawa, J., Goto, T., Goulding, A., Gunn, J.E., Harikane, Y., Hattori, T., Hayashi, M., Hełminiak, K.G., Higuchi, R., Hikage, C., Ho, P.T.P., Hsieh, B.C., Huang, K., Huang, S., Imanishi, M., Iwata, I., Jaelani, A.T., Jian, H.Y., Kashikawa, N., Katayama, N., Kojima, T., Konno, A., Koshida, S., Kusakabe, H., Leauthaud, A., Lee, C.H., Lin, L., Lin, Y.T., Mandelbaum, R., Matsuoka, Y., Medezinski, E., Miyama, S., Momose, R., More, A., More, S., Mukae, S., Murata, R., Murayama, H., Nagao, T., Nakata, F., Niida, M., Niikura, H., Nishizawa, A.J., Oguri, M., Okabe, N., Ono, Y., Onodera, M., Onoue, M., Ouchi, M., Pyo, T.S., Shibuya, T., Shimasaku, K., Simet, M., Speagle, J., Spergel, D.N., Strauss, M.A., Sugahara, Y., Sugiyama, N., Suto, Y., Suzuki, N., Tait, P.J., Takada, M., Terai, T., Toba, Y., Turner, E.L., Uchiyama, H., Umetsu, K., Urata, Y., Usuda, T., Yeh, S., Yuma, S., 2018. First data release of the Hyper Suprime-Cam Subaru Strategic Program. *PASJ* 70, S8. doi:10.1093/pasj/psx081, arXiv:1702.08449.

Akhlaghi, M., Ichikawa, T., 2015. Noise-based Detection and Segmentation of Nebulous Objects. *ApJS* 220, 1. doi:10.1088/0067-0049/220/1/1, arXiv:1505.01664.

Akshaya, M.S., Murthy, J., Ravichandran, S., Henry, R.C., Overduin, J., 2019. Components of the diffuse ultraviolet radiation at high latitudes. *MNRAS* 489, 1120–1126. doi:10.1093/mnras/stz2186, arXiv:1908.02260.

Alina, D., Shomanov, A., Baimukhametova, S., 2022. MaLeFiSenta: Machine Learning for FilamentS Identification and orientation in the ISM. arXiv e-prints , arXiv:2205.00683doi:10.48550/arXiv.2205.00683, arXiv:2205.00683.

André, P., Men'shchikov, A., Bontemps, S., Könyves, V., Motte, F., Schneider, N., Didelon, P., Minier, V., Saraceno, P., Ward-Thompson, D., di Francesco, J., White, G., Molinari, S., Testi, L., Abergel, A., Griffin, M., Henning, T., Royer, P., Merín, B., Vavrek, R., Attard, M., Arzoumanian, D., Wilson, C.D., Ade, P., Aussel, H., Baluteau, J.P., Benedettini, M., Bernard, J.P., Blommaert, J.A.D.L., Cambrésy, L., Cox, P., di Giorgio, A., Hargrave, P., Hennemann, M., Huang, M., Kirk, J., Krause, O., Launhardt, R., Leeks, S., Le Pennec, J., Li, J.Z., Martin, P.G., Maury, A., Olofsson, G., Omont, A., Peretto, N., Pezzuto, S., Prusti, T., Roussel, H., Russeil, D., Sauvage, M., Sibthorpe, B., Sicilia-Aguilar, A., Spinoglio, L., Waelkens, C., Woodcraft, A., Zavagno, A., 2010. From filamentary clouds to prestellar cores to the stellar IMF: Initial highlights from the Herschel Gould Belt Survey. *A&A* 518, L102. doi:10.1051/0004-6361/201014666, arXiv:1005.2618.

Barrena, R., Streblyanska, A., Ferragamo, A., Rubiño-Martín, J.A., Aguado-Barahona, A., Tramonte, D., Génova-Santos, R.T., Hempel, A., Lietzen, H., Aghanim, N., Arnaud, M., Böhringer, H., Chon, G., Democles, J., Dahle, H., Doussis, M., Lasenby, A.N., Mazzotta, P., Melin, J.B., Pointecouteau, E., Pratt, G.W., Rossetti, M., van der Burg, R.F.J., 2018. Optical validation and characterization of Planck PSZ1 sources at the Canary Islands observatories. I. First year of ITP13 observations. *A&A* 616, A42. doi:10.1051/0004-6361/201732315, arXiv:1803.05764.

Bazell, D., Desert, F.X., 1988. Fractal Structure of Interstellar Cirrus. *ApJ* 333, 353. doi:10.1086/166751.

Beattie, J.R., Federrath, C., Klessen, R.S., 2019a. The relation between the true and observed fractal dimensions of turbulent clouds. *MNRAS* 487, 2070–2081. doi:10.1093/mnras/stz1416, arXiv:1905.04979.

Beattie, J.R., Federrath, C., Klessen, R.S., Schneider, N., 2019b. The relation between the turbulent Mach number and observed fractal dimensions of turbulent clouds. *MNRAS* 488, 2493–2502. doi:10.1093/mnras/stz1853, arXiv:1907.01689.

Bernard, J.P., Boulanger, F., Desert, F.X., Giard, M., Helou, G., Puget, J.L., 1994. Dust emission of galactic cirrus from DIRBE observations. *A&A* 291, L5–L8.

Berry, R., Burnell, J., 2005. The Handbook of Astronomical Image Processing. Willmann-Bell. URL: <https://books.google.ru/books?id=00fPPAAACAAJ>.

Bertin, E., Mellier, Y., Radovich, M., Missonnier, G., Didelon, P., Morin, B., 2002. The TERAPIX Pipeline, in: Bohlender, D.A., Durand, D., Handley, T.H. (Eds.), *Astronomical Data Analysis Software and Systems XI*, p. 228.

Bianchi, S., Giovanardi, C., Smith, M.W.L., Fritz, J., Davies, J.I., Haynes, M.P., Giovanelli, R., Baes, M., Bocchio, M., Boissier, S., Boquien, M., Boselli, A., Casasola, V., Clark, C.J.R., De Looze, I., di Serego Alighieri, S., Grossi, M., Jones, A.P., Hughes, T.M., Hunt, L.K., Madden, S., Magrini, L., Pappalardo, C., Ysard, N., Zibetti, S., 2017. The Herschel Virgo Cluster Survey. XX. Dust and gas in the foreground Galactic cirrus. *A&A* 597, A130. doi:10.1051/0004-6361/201629013, arXiv:1609.05941.

Boissier, S., Boselli, A., Voyer, E., Bianchi, S., Pappalardo, C., Guhathakurta, P., Heinis, S., Cortese, L., Duc, P.A., Cuillandre, J.C., Davies, J.I., Smith, M.W.L., 2015. The GALEX Ultraviolet Virgo Cluster Survey (GUViCS). V. Ultraviolet diffuse emission and cirrus properties in the Virgo cluster direction. *A&A* 579, A29. doi:10.1051/0004-6361/201526089, arXiv:1504.06111.

Borlaff, A., Trujillo, I., Román, J., Beckman, J.E., Eliche-Moral, M.C., Infante-Sáinz, R., Lumbreras-Calle, A., de Almagro, R.T.S.M., Gómez-Guijarro, C., Cebríán, M., Dorta, A., Cardiel, N., Akhlaghi, M., Martínez-Lombilla, C., 2019. The missing light of the Hubble Ultra Deep Field. *A&A* 621, A133. doi:10.1051/0004-6361/201834312, arXiv:1810.00002.

Bowes, S.K., Martin, P.G., 2023. Diagnostics from Polarization of Scattered Optical Light from Galactic Infrared Cirrus. *ApJ* 959, 40. doi:10.3847/1538-4357/ad0971, arXiv:2311.01376.

Bradski, G., 2000. The OpenCV Library. *Dr. Dobb's Journal of Software Tools* .

Brandt, T.D., Draine, B.T., 2012. The Spectrum of the Diffuse Galactic Light: The Milky Way in Scattered Light. *ApJ* 744, 129. doi:10.1088/0004-637X/744/2/129, arXiv:1109.4175.

Breiman, L., 1996. Bagging predictors. *Machine Learning* 24, 123–140. URL: <https://api.semanticscholar.org/CorpusID:47328136>.

Breiman, L., 2001. Random Forests. *Machine Learning* 45, 5–32. doi:10.1023/A:1010933404324.

Chellew, B., Brandt, T.D., Hensley, B.S., Draine, B.T., Matthaey, E., 2022. An Optical Spectrum of the Diffuse Galactic Light from BOSS and IRIS. *arXiv e-prints* , arXiv:2201.01378arXiv:2201.01378.

Clark, S.E., Peek, J.E.G., Putman, M.E., 2014. Magnetically Aligned H I Fibers and the Rolling Hough Transform. *ApJ* 789, 82. doi:10.1088/0004-637X/789/1/82, arXiv:1312.1338.

Cortese, L., Bendo, G.J., Isaak, K.G., Davies, J.I., Kent, B.R., 2010. Diffuse far-infrared and ultraviolet emission in the NGC 4435/4438 system: tidal stream or Galactic cirrus? *MNRAS* 403, L26–L30. doi:10.1111/j.1745-3933.2009.00808.x, arXiv:1001.0980.

Cyganek, B., 2012. One-Class Support Vector Ensembles for Image Segmentation and Classification. *Journal of Mathematical Imaging and Vision* 42, 103–117. doi:10.1007/s10851-011-0304-0.

Danieli, S., Lokhorst, D., Zhang, J., Merritt, A., van Dokkum, P., Abraham, R., Conroy, C., Gilhuly, C., Greco, J., Janssens, S., Li, J., Liu, Q., Miller, T.B., Mowla, L., 2020. The Dragonfly Wide Field Survey. I. Telescope, Survey Design, and Data Characterization. *ApJ* 894, 119. doi:10.3847/1538-4357/ab88a8, arXiv:1910.14045.

Davies, J.I., Wilson, C.D., Auld, R., Baes, M., Barlow, M.J., Bendo, G.J., Bock, J.J., Boselli, A., Bradford, M., Buat, V., Castro-Rodriguez, N., Chanial, P., Charlot, S., Ciesla, L., Clements, D.L., Cooray, A., Cormier, D., Cortese, L., Dwek, E., Eales, S.A., Elbaz, D., Galametz, M., Galliano, F., Gear, W.K., Glenn, J., Gomez, H.L., Griffin, M., Hony, S., Isaak, K.G., Levenson, L.R., Lu, N., Madden, S., O'Halloran, B., Okumura, K., Oliver, S., Page, M.J., Panuzzo, P., Papageorgiou, A., Parkin, T.J., Perez-Fournon, I., Pohlen, M., Rangwala, N., Rigby, E.E., Roussel, H., Rykala, A., Sacchi, N., Sauvage, M., Schulz, B., Schirm, M.R.P., Smith, M.W.L., Spinoglio, L., Stevens, J.A., Srinivasan, S., Symeonidis, M., Trichas, M., Vaccari, M., Vigroux, L., Wozniak, H., Wright, G.S., Zeilinger, W.W., 2010. On the origin of M81 group extended dust emission. *MNRAS* 409, 102–108. doi:10.1111/j.1365-2966.2010.17774.x, arXiv:1010.4770.

Duc, P.A., Cuillandre, J.C., Renaud, F., 2018. Revisiting Stephan's Quintet with deep optical images. *MNRAS* 475, L40–L44. doi:10.1093/mnrasl/sly004, arXiv:1712.07145.

Elmegreen, B.G., Falgarone, E., 1996. A Fractal Origin for the Mass Spectrum of Interstellar Clouds. *ApJ* 471, 816. doi:10.1086/178009.

Falgarone, E., Phillips, T.G., Walker, C.K., 1991. The Edges of Molecular Clouds: Fractal Boundaries and Density Structure. *ApJ* 378, 186. doi:10.1086/170419.

Federrath, C., Klessen, R.S., Schmidt, W., 2009. The Fractal Density Structure in Supersonic Isothermal Turbulence: Solenoidal Versus Compressive Energy Injection. *ApJ* 692, 364–374. doi:10.1088/0004-637X/692/1/364, arXiv:0710.1359.

Fliri, J., Trujillo, I., 2016. The IAC Stripe 82 Legacy Project: a wide-area survey for faint surface brightness astronomy. *MNRAS* 456, 1359–1373. doi:10.1093/mnras/stv2686, arXiv:1603.04474.

Fraz, M.M., Remagnino, P., Hoppe, A., Uyyanonvara, B., Rudnicka, A.R., Owen, C.G., Barman, S.A., 2012. An ensemble classification-based approach applied to retinal blood vessel segmentation. *IEEE Transactions on Biomedical Engineering* 59, 2538–2548. doi:10.1109/TBME.2012.2205687.

Friedman, J., Hastie, T., Tibshirani, R., 2000. Additive logistic regression: a statistical view of boosting (With discussion and a rejoinder by the authors). *The Annals of Statistics* 28, 337 – 407. URL: <https://doi.org/10.1214/aos/1016218223>, doi:10.1214/aos/1016218223.

Geller, M.J., Diaferio, A., Kurtz, M.J., 2011. Mapping the Universe: The 2010 Russell Lecture. *AJ* 142, 133. doi:10.1088/0004-6256/142/4/133, arXiv:1110.1380.

Gillmon, K., Shull, J.M., 2006. Molecular Hydrogen in Infrared Cirrus. *ApJ* 636, 908–915. doi:10.1086/498055, arXiv:astro-ph/0507587.

Gontcharov, G.A., Mosenkov, A.V., Savchenko, S.S., Il'in, V.B., Marchuk, A.A., Smirnov, A.A., Usachev, P.A., Polyakov, D.M., Shakespear, Z., 2022. Interstellar Extinction in Galactic Cirri in SDSS Stripe 82. *Astronomy Letters* 48, 503–516. doi:10.1134/S1063773722090031, arXiv:2301.10591.

Gonzalez, R.C., Woods, R.E., 2006. *Digital Image Processing* (3rd Edition). Prentice-Hall, Inc., USA.

Goodfellow, I.J., Pouget-Abadie, J., Mirza, M., Xu, B., Warde-Farley, D., Ozair, S., Courville, A., Bengio, Y., 2014. Generative Adversarial Networks. arXiv e-prints , arXiv:1406.2661doi:10.48550/arXiv.1406.2661, arXiv:1406.2661.

Guan, H., Li, J., Chapman, M., Deng, F., Ji, Z., Yang, X., 2013. Integration of orthoimagery and lidar data for object-based urban thematic mapping using random forests. *International Journal of Remote Sensing* 34, 5166–5186. doi:10.1080/01431161.2013.788261.

Haigh, C., Chamba, N., Venhola, A., Peletier, R., Doorenbos, L., Watkins, M., Wilkinson, M.H.F., 2021. Optimising and comparing source-extraction tools using objective segmentation quality criteria. *A&A* 645, A107. doi:10.1051/0004-6361/201936561, arXiv:2009.07586.

Haikala, L.K., Mattila, K., Bowyer, S., Sasseen, T.P., Lampton, M., Knude, J., 1995. Discovery and Imaging of a Galactic Cirrus Cloud with the Far Ultraviolet Space Telescope. *ApJ* 443, L33. doi:10.1086/187829.

He, K., Gkioxari, G., Dollár, P., Girshick, R., 2017. Mask R-CNN. arXiv e-prints , arXiv:1703.06870doi:10.48550/arXiv.1703.06870, arXiv:1703.06870.

Hennebelle, P., 2013. On the origin of non-self-gravitating filaments in the ISM. *A&A* 556, A153. doi:10.1051/0004-6361/201321292, arXiv:1306.5452.

Hetem, A., J., Lepine, J.R.D., 1993. Fractal 3-D simulations of molecular clouds. *A&A* 270, 451–461.

Howell, S.B., 2006. *Handbook of CCD Astronomy*. Cambridge Observing Handbooks for Research Astronomers. 2 ed., Cambridge University Press.

Ienaka, N., Kawara, K., Matsuoka, Y., Sameshima, H., Oyabu, S., Tsujimoto, T., Peterson, B.A., 2013. Diffuse Galactic Light in the Field of the Translucent High Galactic Latitude Cloud MBM32. *ApJ* 767, 80. doi:10.1088/0004-637X/767/1/80, arXiv:1303.0938.

Jaccard, P., 1901. Distribution de la flore alpine dans le bassin des dranses et dans quelques régions voisines. *Bulletin de la Societe Vaudoise des Sciences Naturelles* 37, 241–72. doi:10.5169/seals-266440.

Joye, W.A., Mandel, E., 2003. New Features of SAOImage DS9, in: Payne, H.E., Jedrzejewski, R.I., Hook, R.N. (Eds.), *Astronomical Data Analysis Software and Systems XII*, p. 489.

Juvela, M., Malinen, J., Montillaud, J., Pelkonen, V.M., Ristorcelli, I., Tóth, L.V., 2018. Galactic cold cores. IX. Column density structures and radiative-transfer modelling. *A&A* 614, A83. doi:10.1051/0004-6361/201630304, arXiv:1801.02419.

Kinattukara, T., Verma, B., 2014. A neural ensemble approach for segmentation and classification of road images, in: Loo, C.K., Yap, K.S., Wong, K.W., Beng Jin, A.T., Huang, K. (Eds.), *Neural Information Processing*, Springer International Publishing, Cham. pp. 183–193.

Kingma, D.P., Ba, J., 2014. Adam: A method for stochastic optimization. *CoRR* abs/1412.6980. URL: <https://api.semanticscholar.org/CorpusID:6628106>.

Kiss, C., Ábrahám, P., Klaas, U., Juvela, M., Lemke, D., 2001. Sky confusion noise in the far-infrared: Cirrus, galaxies and the cosmic far-infrared background. *A&A* 379, 1161–1169. doi:10.1051/0004-6361:20011394, arXiv:astro-ph/0110143.

Kiss, C., Ábrahám, P., Klaas, U., Lemke, D., Héraudeau, P., del Burgo, C., Herbstmeier, U., 2003. Small-scale structure of the galactic cirrus emission. *A&A* 399, 177–185. doi:10.1051/0004-6361:20021787, arXiv:astro-ph/0212094.

Koch, E.W., Rosolowsky, E.W., 2015. Filament identification through mathematical morphology. *MNRAS* 452, 3435–3450. doi:10.1093/mnras/stv1521, arXiv:1507.02289.

Konstandin, L., Schmidt, W., Girichidis, P., Peters, T., Shetty, R., Klessen, R.S., 2016. Mach number study of supersonic turbulence: the properties of the density field. *MNRAS* 460, 4483–4491. doi:10.1093/mnras/stw1313, arXiv:1506.03834.

Kowal, G., Lazarian, A., 2007. Scaling Relations of Compressible MHD Turbulence. *ApJ* 666, L69–L72. doi:10.1086/521788, arXiv:0705.2464.

Koyama, H., Inutsuka, S.I., 2000. Molecular cloud formation in shock-compressed layers. *The Astrophysical Journal* 532, 980–993. URL: <https://doi.org/10.1086/308594>, doi:10.1086/308594.

Laureijs, R., Amiaux, J., Arduini, S., Auguères, J.L., Brinchmann, J., Cole, R., Cropper, M., Dabin, C., Duvet, L., Ealet, A., Garilli, B., Gondoin, P., Guzzo, L., Hoar, J., Hoekstra, H., Holmes, R., Kitching, T., Maciaszek, T., Mellier, Y., Pasian, F., Percival, W., Rhodes, J., Saavedra Criado, G., Sauvage, M., Scaramella, R., Valenziano, L., Warren, S., Bender, R., Castander, F., Cimatti, A., Le Fèvre, O., Kurki-Suonio, H., Levi, M., Lilje, P., Meylan, G., Nichol, R., Pedersen, K., Popa, V., Rebolo Lopez, R., Rix, H.W., Rottgering, H., Zeilinger, W., Grupp, F., Hudelot, P., Massey, R., Meneghetti, M., Miller, L., Paltani, S., Paulin-Henriksson, S., Pires, S., Saxton, C., Schrabbach, T., Seidel, G., Walsh, J., Aghanim, N., Amendola, L., Bartlett, J., Baccigalupi, C., Beaulieu, J.P., Benabed, K., Cuby, J.G., Elbaz, D., Fosalba, P., Gavazzi, G., Helmi, A., Hook, I., Irwin, M., Kneib, J.P., Kunz, M., Mannucci, F., Moscardini, L., Tao, C., Teyssier, R., Weller, J., Zamorani, G., Zapatero Osorio, M.R., Boulade, O., Foumond, J.J., Di Giorgio, A., Guttridge, P., James, A., Kemp, M., Martignac, J., Spencer, A., Walton, D., Blümchen, T., Bonoli, C., Bortoletto, F., Cerna, C., Corcione, L., Fabron, C., Jahnke, K., Ligori, S., Madrid, F., Martin, L.,

Morgante, G., Pamplona, T., Prieto, E., Riva, M., Toledo, R., Trifoglio, M., Zerbi, F., Abdalla, F., Douspis, M., Grenet, C., Borgani, S., Bouwens, R., Courbin, F., Delouis, J.M., Dubath, P., Fontana, A., Frailis, M., Grazian, A., Koppenhöfer, J., Mansutti, O., Melchior, M., Mignoli, M., Mohr, J., Neissner, C., Noddle, K., Poncet, M., Scodéggi, M., Serrano, S., Shane, N., Starck, J.L., Surace, C., Taylor, A., Verdoes-Kleijn, G., Vuerli, C., Williams, O.R., Zacchei, A., Altieri, B., Escudero Sanz, I., Kohley, R., Oosterbroek, T., Astier, P., Bacon, D., Bardelli, S., Baugh, C., Bellagamba, F., Benoist, C., Bianchi, D., Biviano, A., Branchini, E., Carbone, C., Cardone, V., Clements, D., Colombi, S., Conselice, C., Cresci, G., Deacon, N., Dunlop, J., Fedeli, C., Fontanot, F., Franzetti, P., Giocoli, C., Garcia-Bellido, J., Gow, J., Heavens, A., Hewett, P., Heymans, C., Holland, A., Huang, Z., Ilbert, O., Joachimi, B., Jennins, E., Kerins, E., Kiessling, A., Kirk, D., Kotak, R., Krause, O., Lahav, O., van Leeuwen, F., Lesgourgues, J., Lombardi, M., Magliocchetti, M., Maguire, K., Majerotto, E., Maoli, R., Marulli, F., Maurogordato, S., McCracken, H., McLure, R., Melchiorri, A., Merson, A., Moresco, M., Nonino, M., Norberg, P., Peacock, J., Pello, R., Penny, M., Pettorino, V., Di Porto, C., Pozzetti, L., Quercellini, C., Radovich, M., Rassat, A., Roche, N., Ronayette, S., Rossetti, E., Sartoris, B., Schneider, P., Semboloni, E., Serjeant, S., Simpson, F., Skordis, C., Smadja, G., Smartt, S., Spano, P., Spiro, S., Sullivan, M., Tilquin, A., Trotta, R., Verde, L., Wang, Y., Williger, G., Zhao, G., Zoubian, J., Zucca, E., 2011. Euclid Definition Study Report. arXiv e-prints , arXiv:1110.3193arXiv:1110.3193.

Laureijs, R.J., Mattila, K., Schnur, G., 1987. IRAS and optical observations of the high-latitude dust cloud Lynds 1642. *A&A* 184, 269–278.

Liu, Q., Abraham, R., Gilhuly, C., van Dokkum, P., Martin, P.G., Li, J., Greco, J.P., Lokhorst, D., Chen, S., Danieli, S., Keim, M.A., Merritt, A., Miller, T.B., Pasha, I., Polzin, A., Shen, Z., Zhang, J., 2022. A Method to Characterize the Wide-angle Point-Spread Function of Astronomical Images. *ApJ* 925, 219. doi:10.3847/1538-4357/ac32c6, arXiv:2110.11598.

Liu, Q., Abraham, R., Martin, P.G., Bowman, W.P., Dokkum, P.v., Danieli, S., Patel, E., Janssens, S.R., Shen, Z., Chen, S., Karunakaran, A., Keim, M.A., Lokhorst, D., Pasha, I., Welch, D.L., 2025. Fuzzy Galaxies or Cirrus? Decomposition of Galactic Cirrus in Deep Wide-field Images. *ApJ* 979, 175. doi:10.3847/1538-4357/ad9b25.

Low, F.J., Beintema, D.A., Gautier, T.N., Gillett, F.C., Beichman, C.A., Neugebauer, G., Young, E., Aumann, H.H., Boggess, N., Emerson, J.P., Habing, H.J., Hauser, M.G., Houck, J.R., Rowan-Robinson, M., Soifer, B.T., Walker, R.G., Wesselius, P.R., 1984. Infrared cirrus: new components of the extended infrared emission. *ApJ* 278, L19–L22. doi:10.1086/184213.

LSST Science Collaboration, Abell, P.A., Allison, J., Anderson, S.F., Andrew, J.R., Angel, J.R.P., Armus, L., Arnett, D., Asztalos, S.J., Axelrod, T.S., Bailey, S., Ballantyne, D.R., Bankert, J.R., Barkhouse, W.A., Barr, J.D., Barrientos, L.F., Barth, A.J., Bartlett, J.G., Becker, A.C., Becla, J., Beers, T.C., Bernstein, J.P., Biswas, R., Blanton, M.R., Bloom, J.S., Bochanski, J.J., Boeshaar, P., Borne, K.D., Bradac, M., Brandt, W.N., Bridge, C.R., Brown, M.E., Brunner, R.J., Bullock, J.S., Burgasser, A.J., Burge, J.H., Burke, D.L., Cargile, P.A., Chandrasekharan, S., Chartas, G., Chesley, S.R., Chu, Y.H., Cinabro, D., Claire, M.W., Claver, C.F., Clowe, D., Connolly, A.J., Cook, K.H., Cooke, J., Cooray, A., Covey, K.R., Culliton, C.S., de Jong, R., de Vries, W.H., Debattista, V.P., Delgado, F., Dell'Antonio, I.P., Dhital, S., Di Stefano, R., Dickinson, M., Dilday, B., Djorgovski, S.G., Dobler, G., Donalek, C., Dubois-Felsmann, G., Durech, J., Eliasdottir, A., Eracleous, M., Eyer, L., Falco, E.E., Fan, X., Fassnacht, C.D., Ferguson, H.C., Fernandez, Y.R., Fields, B.D., Finkbeiner, D., Figueroa, E.E., Fox, D.B., Francke, H., Frank, J.S., Frieman, J., Fromenteau, S., Furqan, M., Galaz, G., Gal-Yam, A., Garnavich, P., Gawiser, E., Geary, J., Gee, P., Gibson, R.R., Gilmore, K., Grace, E.A., Green, R.F., Gressler, W.J., Grillmair, C.J., Habib, S., Haggerty, J.S., Hamuy, M., Harris, A.W., Hawley, S.L., Heavens, A.F., Hebb, L., Henry, T.J., Hileman, E., Hilton, E.J., Hoadley, K., Holberg, J.B., Holman, M.J., Howell, S.B., Infante, L., Ivezić, Z., Jacoby, S.H., Jain, B., R., Jedicke, Jee, M.J., Garrett Jernigan, J., Jha, S.W., Johnston, K.V., Jones, R.L., Juric, M., Kaasalainen, M., Stylianis, Kafka, Kahn, S.M., Kaib, N.A., Kalirai, J., Kantor, J., Kasliwal, M.M., Keeton, C.R., Kessler, R., Knezevic, Z., Kowalski, A., Krabbendam, V.L., Krughoff, K.S., Kulkarni, S., Kuhlman, S., Lacy, M., Lepine, S., Liang, M., Lien, A., Lira, P., Long, K.S., Lorenz, S., Lotz, J.M., Lupton, R.H., Lutz, J., Macri, L.M., Mahabal, A.A., Mandelbaum, R., Marshall, P., May, M., McGehee, P.M., Meadows, B.T., Meert, A., Milani, A., Miller, C.J., Miller, M., Mills, D., Minniti, D., Monet, D., Mukadam, A.S., Nakar, E., Neill, D.R., Newman, J.A., Nikolaev, S., Nordby, M., O'Connor, P., Oguri, M., Oliver, J., Olivier, S.S., Olsen, J.K., Olsen, K., Olszewski, E.W., Oluseyi, H., Padilla, N.D., Parker,

A., Pepper, J., Peterson, J.R., Petry, C., Pinto, P.A., Pizagno, J.L., Popescu, B., Prsa, A., Radcka, V., Raddick, M.J., Rasmussen, A., Rau, A., Rho, J., Rhoads, J.E., Richards, G.T., Ridgway, S.T., Robertson, B.E., Roskar, R., Saha, A., Sarajedini, A., Scannapieco, E., Schalk, T., Schindler, R., Schmidt, S., Schmidt, S., Schneider, D.P., Schumacher, G., Scranton, R., Sebag, J., Seppala, L.G., Shemmer, O., Simon, J.D., Sivertz, M., Smith, H.A., Allyn Smith, J., Smith, N., Spitz, A.H., Stanford, A., Stassun, K.G., Strader, J., Strauss, M.A., Stubbs, C.W., Sweeney, D.W., Szalay, A., Szkody, P., Takada, M., Thorman, P., Trilling, D.E., Trimble, V., Tyson, A., Van Berg, R., Vanden Berk, D., VanderPlas, J., Verde, L., Vrsnak, B., Walkowicz, L.M., Wandelt, B.D., Wang, S., Wang, Y., Warner, M., Wechsler, R.H., West, A.A., Wiecha, O., Williams, B.F., Willman, B., Wittman, D., Wolff, S.C., Wood-Vasey, W.M., Wozniak, P., Young, P., Zentner, A., Zhan, H., 2009. LSST Science Book, Version 2.0. arXiv e-prints , arXiv:0912.0201arXiv:0912.0201.

Marchuk, A.A., Smirnov, A.A., Mosenkov, A.V., Il'in, V.B., Gontcharov, G.A., Savchenko, S.S., Román, J., 2021. Fractal dimension of optical cirrus in Stripe82. *MNRAS* 508, 5825–5841. doi:10.1093/mnras/stab2846, arXiv:2109.14034.

Marchuk, A.A., Smirnov, A.A., Sotnikova, N.Y., Bunakalya, D.A., Savchenko, S.S., Reshetnikov, V.P., Usachev, P.A., Tikhonenko, I.S., Zozulia, V.D., Zakharova, D.A., 2022. B/PS bulges in DESI Legacy edge-on galaxies - I. Sample building. *MNRAS* 512, 1371–1390. doi:10.1093/mnras/stac599, arXiv:2203.01154.

Martin, P.G., Miville-Deschénes, M.A., Roy, A., Bernard, J.P., Molinari, S., Billot, N., Brunt, C., Calzoletti, L., Digiorgio, A.M., Elia, D., Faustini, F., Joncas, G., Mottram, J.C., Natoli, P., Noriega-Crespo, A., Paladini, R., Robitaille, J.F., Strafella, F., Traficante, A., Veneziani, M., 2010. Direct estimate of cirrus noise in Herschel Hi-GAL images. *A&A* 518, L105. doi:10.1051/0004-6361/201014684, arXiv:1005.3076.

Mattila, K., 1979. Optical extinction and surface brightness observations of the dark nebulae Lynds 134 and Lynds 1778/1780. *A&A* 78, 253–263.

Mattila, K., Väisänen, P., Lehtinen, K., Haikala, L., Haas, M., 2023. Light and colour of cirrus, translucent, and opaque dust in the high-latitude area of LDN 1642. *MNRAS* 524, 2797–2813. doi:10.1093/mnras/stad1940, arXiv:2306.16467.

Men'shchikov, A., 2013. A multi-scale filament extraction method: getfilaments. *A&A* 560, A63. doi:10.1051/0004-6361/201321885, arXiv:1309.2170.

Mienye, I.D., Sun, Y., 2022. A survey of ensemble learning: Concepts, algorithms, applications, and prospects. *IEEE Access* 10, 99129–99149. doi:10.1109/ACCESS.2022.3207287.

Miville-Deschénes, M.A., Duc, P.A., Marleau, F., Cuillandre, J.C., Didelon, P., Gwyn, S., Karabal, E., 2016. Probing interstellar turbulence in cirrus with deep optical imaging: no sign of energy dissipation at 0.01 pc scale. *A&A* 593, A4. doi:10.1051/0004-6361/201628503, arXiv:1605.08360.

Molinari, S., Swinyard, B., Bally, J., Barlow, M., Bernard, J.P., Martin, P., Moore, T., Noriega-Crespo, A., Plume, R., Testi, L., Zavagno, A., Abergel, A., Ali, B., André, P., Baluteau, J.P., Benedettini, M., Berné, O., Billot, N.P., Blommaert, J., Bontemps, S., Boulanger, F., Brand, J., Brunt, C., Burton, M., Campeggio, L., Carey, S., Caselli, P., Cesaroni, R., Cernicharo, J., Chakrabarti, S., Chrysostomou, A., Codella, C., Cohen, M., Compiegne, M., Davis, C.J., de Bernardis, P., de Gasperis, G., Francesco, J.D., di Giorgio, A.M., Elia, D., Faustini, F., Fischera, J.F., Fukui, Y., Fuller, G.A., Ganga, K., Garcia-Lario, P., Giard, M., Giardino, G., Glenn, J., Goldsmith, P., Griffin, M., Hoare, M., Huang, M., Jiang, B., Joblin, C., Joncas, G., Juvela, M., Kirk, J., Lagache, G., Li, J.Z., Lim, T.L., Lord, S.D., Lucas, P.W., Maiolo, B., Marengo, M., Marshall, D., Masi, S., Massi, F., Matsuura, M., Meny, C., Minier, V., Miville-Deschénes, M.A., Montier, L., Motte, F., Müller, T.G., Natoli, P., Neves, J., Olmi, L., Paladini, R., Paradis, D., Pestalozzi, M., Pezzuto, S., Piacentini, F., Pomarès, M., Popescu, C.C., Reach, W.T., Richer, J., Ristorcelli, I., Roy, A., Royer, P., Russeil, D., Saraceno, P., Sauvage, M., Schilke, P., Schneider-Bontemps, N., Schuller, F., Schultz, B., Shepherd, D.S., Sibthorpe, B., Smith, H.A., Smith, M.D., Spinoglio, L., Stamatellos, D., Strafella, F., Stringfellow, G., Sturm, E., Taylor, R., Thompson, M.A., Tuffs, R.J., Umana, G., Valenziano, L., Vavrek, R., Viti, S., Waelkens, C., Ward-Thompson, D., White, G., Wyrowski, F., Yorke, H.W., Zhang, Q., 2010. Hi-GAL:

The herschel infrared galactic plane survey. Publications of the Astronomical Society of the Pacific 122, 314–325. URL: <https://doi.org/10.1086/651314>, doi:10.1086/651314.

Moradi, M., Chen, Y., Du, X., Seddon, J.M., 2023. Deep ensemble learning for automated non-advanced and classification using optimized retinal layer segmentation and sd-oct scans. Computers in biology and medicine 154, 106512. URL: <https://api.semanticscholar.org/CorpusID:255658002>.

Nagai, T., ichiro Inutsuka, S., Miyama, S.M., 1998. An origin of filamentary structure in molecular clouds. The Astrophysical Journal 506, 306–322. URL: <https://doi.org/10.1086/306249>, doi:10.1086/306249.

Nanni, L., Lumini, A., Fantozzi, C., 2023. Exploring the potential of ensembles of deep learning networks for image segmentation. Inf. 14, 657. URL: <https://api.semanticscholar.org/CorpusID:266216418>.

Nun, I., Protopapas, P., Sim, B., Chen, W., 2016. Ensemble Learning Method for Outlier Detection and its Application to Astronomical Light Curves. AJ 152, 71. doi:10.3847/0004-6256/152/3/71.

Onishi, Y., Sano, K., Matsuura, S., Jeong, W.S., Pyo, J., Kim, I.J., Seo, H.J., Han, W., Lee, D., Moon, B., Park, W., Park, Y., Kim, M., Matsumoto, T., Matsuura, H., Nakagawa, T., Tsumura, K., Shirahata, M., Arai, T., Ienaka, N., 2018. MIRIS observation of near-infrared diffuse Galactic light. PASJ 70, 76. doi:10.1093/pasj/psy070, [arXiv:1806.08891](https://arxiv.org/abs/1806.08891).

Padoan, P., Juvela, M., Goodman, A.A., Nordlund, Å., 2001. The Turbulent Shock Origin of Proto-Stellar Cores. ApJ 553, 227–234. doi:10.1086/320636, [arXiv:astro-ph/0011122](https://arxiv.org/abs/astro-ph/0011122).

Pagliaro, A., Cusumano, G., La Barbera, A., La Parola, V., Lombardi, S., 2023. Application of machine learning ensemble methods to astri mini-array cherenkov event reconstruction. Applied Sciences 13. URL: <https://www.mdpi.com/2076-3417/13/14/8172>, doi:10.3390/app13148172.

Pénin, A., Lagache, G., Noriega-Crespo, A., Grain, J., Miville-Deschénes, M.A., Ponthieu, N., Martin, P., Blagrave, K., Lockman, F.J., 2012. An accurate measurement of the anisotropies and mean level of the cosmic infrared background at 100 μ m and 160 μ m. A&A 543, A123. doi:10.1051/0004-6361/201015929, [arXiv:1105.1463](https://arxiv.org/abs/1105.1463).

Planck Collaboration, Abergel, A., Ade, P.A.R., Aghanim, N., Alves, M.I.R., Aniano, G., Arnaud, M., Ashdown, M., Aumont, J., Baccigalupi, C., Banday, A.J., Barreiro, R.B., Bartlett, J.G., Battaner, E., Benabed, K., Benoit-Lévy, A., Bernard, J.P., Bersanelli, M., Bielewicz, P., Bobin, J., Bonaldi, A., Bond, J.R., Bouchet, F.R., Boulanger, F., Burigana, C., Cardoso, J.F., Catalano, A., Chamballu, A., Chiang, H.C., Christensen, P.R., Clements, D.L., Colombi, S., Colombo, L.P.L., Couchot, F., Crill, B.P., Cuttaia, F., Danese, L., Davis, R.J., de Bernardis, P., de Rosa, A., de Zotti, G., Delabrouille, J., Désert, F.X., Dickinson, C., Diego, J.M., Dole, H., Donzelli, S., Doré, O., Douspis, M., Dupac, X., Efstathiou, G., Enßlin, T.A., Eriksen, H.K., Falgarone, E., Finelli, F., Forni, O., Frailis, M., Franceschi, E., Galeotta, S., Ganga, K., Ghosh, T., Giard, M., Giraud-Héraud, Y., González-Nuevo, J., Górski, K.M., Gregorio, A., Gruppuso, A., Guillet, V., Hansen, F.K., Harrison, D., Helou, G., Henrot-Versillé, S., Hernández-Monteagudo, C., Herranz, D., Hildebrandt, S.R., Hivon, E., Hobson, M., Holmes, W.A., Hornstrup, A., Hovest, W., Huffenberger, K.M., Jaffe, A.H., Jaffe, T.R., Joncas, G., Jones, A., Jones, W.C., Juvela, M., Kalberla, P., Keihänen, E., Kerp, J., Keskitalo, R., Kisner, T.S., Kneissl, R., Knoche, J., Kunz, M., Kurki-Suonio, H., Lagache, G., Lähteenmäki, A., Lamarre, J.M., Lasenby, A., Lawrence, C.R., Leonardi, R., Levrier, F., Liguori, M., Lilje, P.B., Linden-Vørnle, M., López-Caniego, M., Lubin, P.M., Macías-Pérez, J.F., Maffei, B., Maino, D., Mandolesi, N., Maris, M., Marshall, D.J., Martin, P.G., Martínez-González, E., Masi, S., Massardi, M., Matarrese, S., Mazzotta, P., Melchiorri, A., Mendes, L., Mennella, A., Migliaccio, M., Mitra, S., Miville-Deschénes, M.A., Moneti, A., Montier, L., Morgante, G., Mortlock, D., Munshi, D., Murphy, J.A., Naselsky, P., Nati, F., Natoli, P., Noviello, F., Novikov, D., Novikov, I., Oxborrow, C.A., Pagano, L., Pajot, F., Paoletti, D., Pasian, F., Perdereau, O., Perotto, L., Perrotta, F., Piacentini, F., Piat, M., Pierpaoli, E., Pietrobon, D., Plaszczynski, S., Pointecouteau, E., Polenta, G., Ponthieu, N., Popa, L., Pratt, G.W., Prunet, S., Puget, J.L., Rachen, J.P., Reach, W.T., Rebolo, R., Reinecke, M., Remazeilles, M., Renault, C., Ricciardi, S., Riller, T., Ristorcelli, I., Rocha, G., Rosset, C., Roudier, G., Rusholme, B., Sandri, M., Savini, G., Spencer, L.D., Starck, J.L., Sureau, F., Sutton, D., Suur-Uski, A.S., Sygnet, J.F., Tauber, J.A., Terenzi, L., Toffolatti, L., Tomasi, M., Tristram, M., Tucci, M., Umana, G., Valenziano, L., Valiviita, J., Van

Tent, B., Verstraete, L., Vielva, P., Villa, F., Wade, L.A., Wandelt, B.D., Winkel, B., Yvon, D., Zacchei, A., Zonca, A., 2014. Planck intermediate results. XVII. Emission of dust in the diffuse interstellar medium from the far-infrared to microwave frequencies. *A&A* 566, A55. doi:10.1051/0004-6361/201323270, arXiv:1312.5446.

Planck Collaboration, Adam, R., Ade, P.A.R., Aghanim, N., Alves, M.I.R., Arnaud, M., Arzoumanian, D., Ashdown, M., Aumont, J., Baccigalupi, C., Banday, A.J., Barreiro, R.B., Bartolo, N., Battaner, E., Benabed, K., Benoit-Lévy, A., Bernard, J.P., Bersanelli, M., Bielewicz, P., Bonaldi, A., Bonavera, L., Bond, J.R., Borrill, J., Bouchet, F.R., Boulanger, F., Bracco, A., Burigana, C., Butler, R.C., Calabrese, E., Cardoso, J.F., Catalano, A., Chamballu, A., Chiang, H.C., Christensen, P.R., Colombi, S., Colombo, L.P.L., Combet, C., Couchot, F., Crill, B.P., Curto, A., Cuttaia, F., Danese, L., Davies, R.D., Davis, R.J., de Bernardis, P., de Rosa, A., de Zotti, G., Delabrouille, J., Dickinson, C., Diego, J.M., Dole, H., Donzelli, S., Doré, O., Douspis, M., Ducout, A., Dupac, X., Efstathiou, G., Elsner, F., Enßlin, T.A., Eriksen, H.K., Falgarone, E., Ferrière, K., Finelli, F., Forni, O., Frailis, M., Fraisse, A.A., Franceschi, E., Frejsel, A., Galeotta, S., Galli, S., Ganga, K., Ghosh, T., Giard, M., Gjerløw, E., González-Nuevo, J., Górski, K.M., Gregorio, A., Gruppuso, A., Guillet, V., Hansen, F.K., Hanson, D., Harrison, D.L., Henrot-Versillé, S., Hernández-Monteagudo, C., Herranz, D., Hildebrandt, S.R., Hivon, E., Hobson, M., Holmes, W.A., Hovest, W., Huffenberger, K.M., Hurier, G., Jaffe, A.H., Jaffe, T.R., Jones, W.C., Juvela, M., Keihänen, E., Keskitalo, R., Kisner, T.S., Kneissl, R., Knoche, J., Kunz, M., Kurki-Suonio, H., Lagache, G., Lamarre, J.M., Lasenby, A., Lattanzi, M., Lawrence, C.R., Leonardi, R., Levrier, F., Liguori, M., Lilje, P.B., Linden-Vørnle, M., López-Caniego, M., Lubin, P.M., Macías-Pérez, J.F., Maffei, B., Maino, D., Mandolesi, N., Maris, M., Marshall, D.J., Martin, P.G., Martínez-González, E., Masi, S., Matarrese, S., Mazzotta, P., Melchiorri, A., Mendes, L., Mennella, A., Migliaccio, M., Miville-Deschénes, M.A., Moneti, A., Montier, L., Morgante, G., Mortlock, D., Munshi, D., Murphy, J.A., Naselsky, P., Natoli, P., Nørgaard-Nielsen, H.U., Noviello, F., Novikov, D., Novikov, I., Oppermann, N., Oxborrow, C.A., Pagano, L., Pajot, F., Paoletti, D., Pasian, F., Perdereau, O., Perotto, L., Perrotta, F., Pettorino, V., Piacentini, F., Piat, M., Plaszczynski, S., Pointecouteau, E., Polenta, G., Ponthieu, N., Popa, L., Pratt, G.W., Prunet, S., Puget, J.L., Rachen, J.P., Reach, W.T., Reinecke, M., Remazeilles, M., Renault, C., Ristorcelli, I., Rocha, G., Roudier, G., Rubiño-Martín, J.A., Rusholme, B., Sandri, M., Santos, D., Savini, G., Scott, D., Soler, J.D., Spencer, L.D., Stolyarov, V., Sudiwala, R., Sunyaev, R., Sutton, D., Suur-Uski, A.S., Sygnet, J.F., Tauber, J.A., Terenzi, L., Toffolatti, L., Tomasi, M., Tristram, M., Tucci, M., Umana, G., Valenziano, L., Valiviita, J., Van Tent, B., Vielva, P., Villa, F., Wade, L.A., Wandelt, B.D., Wehus, I.K., Wiesemeyer, H., Yvon, D., Zacchei, A., Zonca, A., 2016. Planck intermediate results. XXXII. The relative orientation between the magnetic field and structures traced by interstellar dust. *A&A* 586, A135. doi:10.1051/0004-6361/201425044, arXiv:1409.6728.

Planck Collaboration, Ade, P.A.R., Aghanim, N., Arnaud, M., Ashdown, M., Aumont, J., Baccigalupi, C., Balbi, A., Banday, A.J., Barreiro, R.B., Bartlett, J.G., Battaner, E., Benabed, K., Benoît, A., Bernard, J.P., Bersanelli, M., Bhatia, R., Bock, J.J., Bonaldi, A., Bond, J.R., Borrill, J., Bouchet, F.R., Boulanger, F., Bucher, M., Burigana, C., Cabella, P., Cantalupo, C.M., Cardoso, J.F., Catalano, A., Cayón, L., Challinor, A., Chamballu, A., Chiang, L.Y., Christensen, P.R., Clements, D.L., Colombi, S., Couchot, F., Coulais, A., Crill, B.P., Cuttaia, F., Danese, L., Davies, R.D., de Bernardis, P., de Gasperis, G., de Rosa, A., de Zotti, G., Delabrouille, J., Delouis, J.M., Désert, F.X., Dickinson, C., Doi, Y., Donzelli, S., Doré, O., Dörl, U., Douspis, M., Dupac, X., Efstathiou, G., Enßlin, T.A., Falgarone, E., Finelli, F., Forni, O., Frailis, M., Franceschi, E., Galeotta, S., Ganga, K., Giard, M., Giardino, G., Giraud-Héraud, Y., González-Nuevo, J., Górski, K.M., Gratton, S., Gregorio, A., Gruppuso, A., Hansen, F.K., Harrison, D., Helou, G., Henrot-Versillé, S., Herranz, D., Hildebrandt, S.R., Hivon, E., Hobson, M., Holmes, W.A., Hovest, W., Hoyland, R.J., Huffenberger, K.M., Ikeda, N., Jaffe, A.H., Jones, W.C., Juvela, M., Keihänen, E., Keskitalo, R., Kisner, T.S., Kitamura, Y., Kneissl, R., Knox, L., Kurki-Suonio, H., Lagache, G., Lamarre, J.M., Lasenby, A., Laureijs, R.J., Lawrence, C.R., Leach, S., Leonardi, R., Leroy, C., Linden-Vørnle, M., López-Caniego, M., Lubin, P.M., Macías-Pérez, J.F., MacTavish, C.J., Maffei, B., Malinen, J., Mandolesi, N., Mann, R., Maris, M., Marshall, D.J., Martin, P., Martínez-González, E., Masi, S., Matarrese, S., Matthai, F., Mazzotta, P., McGehee, P., Melchiorri, A., Mendes, L., Mennella, A., Meny, C., Mitra, S., Miville-Deschénes, M.A., Moneti, A., Montier, L., Morgante, G., Mortlock, D., Munshi, D., Murphy, A., Naselsky, P., Nati, F., Natoli, P., Netterfield, C.B., Nørgaard-Nielsen, H.U., Noviello, F., Novikov, D., Novikov, I., Osborne, S., Pagani, L., Pajot, F., Paladini, R., Pasian, F., Patanchon, G., Pelkonen, V.M., Perdereau, O., Perotto, L., Perrotta, F., Piacentini, F., Piat, M., Plaszczynski, S., Pointecouteau, E., Polenta, G., Ponthieu, N., Poutanen, T., Prézeau, G., Prunet, S., Puget, J.L., Reach, W.T., Rebolo, R., Reinecke, M., Renault, C., Ricciardi, S., Riller, T., Ristorcelli, I., Rocha, G.,

Rosset, C., Rowan-Robinson, M., Rubiño-Martín, J.A., Rusholme, B., Sandri, M., Santos, D., Savini, G., Scott, D., Seiffert, M.D., Smoot, G.F., Starck, J.L., Stivoli, F., Stolyarov, V., Sudiwala, R., Sygnet, J.F., Tauber, J.A., Terenzi, L., Toffolatti, L., Tomasi, M., Torre, J.P., Toth, V., Tristram, M., Tuovinen, J., Umana, G., Valenziano, L., Vielva, P., Villa, F., Vittorio, N., Wade, L.A., Wandelt, B.D., Ysard, N., Yvon, D., Zacchei, A., Zonca, A., 2011. Planck early results. XXII. The submillimetre properties of a sample of Galactic cold clumps. *A&A* 536, A22. doi:10.1051/0004-6361/201116481, arXiv:1101.2034.

Priyadarshini, I., Puri, V., 2021. A convolutional neural network (CNN) based ensemble model for exoplanet detection. *Earth Science Informatics* 14, 735–747. doi:10.1007/s12145-021-00579-5.

Qurat-Ul-Ain, Q.U.A., Latif, G., Kazmi, S.B., Jaffar, M.A., Mirza, A.M., 2010. Classification and segmentation of brain tumor using texture analysis, in: Proceedings of the 9th WSEAS International Conference on Artificial Intelligence, Knowledge Engineering and Data Bases, World Scientific and Engineering Academy and Society (WSEAS), Stevens Point, Wisconsin, USA. p. 147–155.

Ren, Y., Zhang, L., Suganthan, P.N., 2016. Ensemble classification and regression-recent developments, applications and future directions [review article]. *IEEE Computational Intelligence Magazine* 11, 41–53. URL: <https://api.semanticscholar.org/CorpusID:14010214>.

Richards, F., Paiement, A., Xie, X., Sola, E., Duc, P.A., 2024. Multi-scale gridded Gabor attention for cirrus segmentation. arXiv e-prints , arXiv:2407.08852doi:10.48550/arXiv.2407.08852, arXiv:2407.08852.

Román, J., Trujillo, I., Montes, M., 2020. Galactic cirri in deep optical imaging. *A&A* 644, A42. doi:10.1051/0004-6361/201936111, arXiv:1907.00978.

Ronneberger, O., Fischer, P., Brox, T., 2015. U-Net: Convolutional Networks for Biomedical Image Segmentation. arXiv e-prints , arXiv:1505.04597arXiv:1505.04597.

Rudick, C.S., Mihos, J.C., Harding, P., Feldmeier, J.J., Janowiecki, S., Morrison, H.L., 2010. Optical Colors of Intracluster Light in the Virgo Cluster Core. *ApJ* 720, 569–580. doi:10.1088/0004-637X/720/1/569, arXiv:1003.4500.

Salji, C.J., Richer, J.S., Buckle, J.V., di Francesco, J., Hatchell, J., Hogerheijde, M., Johnstone, D., Kirk, H., Ward-Thompson, D., JCMT GBS Consortium, 2015. The JCMT Gould Belt Survey: properties of star-forming filaments in Orion A North. *MNRAS* 449, 1782–1796. doi:10.1093/mnras/stv369.

Sánchez, N., Alfaro, E.J., Pérez, E., 2005. The Fractal Dimension of Projected Clouds. *ApJ* 625, 849–856. doi:10.1086/429553, arXiv:astro-ph/0501573.

Sandage, A., 1976. High-latitude reflection nebulosities illuminated by the galactic plane. *AJ* 81, 954. doi:10.1086/111975.

Sandler, M., Howard, A., Zhu, M., Zhmoginov, A., Chen, L.C., 2018. MobileNetV2: Inverted Residuals and Linear Bottlenecks. arXiv e-prints , arXiv:1801.04381arXiv:1801.04381.

Savchenko, S.S., Makarov, D.I., Antipova, A.V., Tikhonenko, I.S., 2024. Search for the edge-on galaxies using an artificial neural network. *Astronomy and Computing* 46, 100771. doi:10.1016/j.ascom.2023.100771, arXiv:2312.02742.

Schisano, E., Molinari, S., Elia, D., Benedettini, M., Olmi, L., Pezzuto, S., Traficante, A., Brescia, M., Cavuoti, S., di Giorgio, A.M., Liu, S.J., Moore, T.J.T., Noriega-Crespo, A., Riccio, G., Baldeschi, A., Becciani, U., Peretto, N., Merello, M., Vitello, F., Zavagno, A., Beltrán, M.T., Cambrésy, L., Eden, D.J., Li Causi, G., Molinaro, M., Palmeirim, P., Sciacca, E., Testi, L., Umana, G., Whitworth, A.P., 2020. The Hi-GAL catalogue of dusty filamentary structures in the Galactic plane. *MNRAS* 492, 5420–5456. doi:10.1093/mnras/stz3466, arXiv:1912.04020.

Serra, J., Serra, J., 1982. Image Analysis and Mathematical Morphology. *Image Analysis and Mathematical Morphology*, Academic Press. URL: <https://books.google.ru/books?id=BpdTAAAYAAJ>.

Smirnov, A.A., Savchenko, S.S., Poliakov, D.M., Marchuk, A.A., Mosenkov, A.V., Il'in, V.B., Gontcharov, G.A., Román, J., Seguine, J., 2023. Prospects for future studies using deep imaging: analysis of individual Galactic cirrus filaments. *MNRAS* 519, 4735–4752. doi:10.1093/mnras/stac3765, arXiv:2301.12410.

Soler, J.D., Miville-Deschénes, M.A., Molinari, S., Klessen, R.S., Hennebelle, P., Testi, L., McClure-Griffiths, N.M., Beuther, H., Elia, D., Schisano, E., Traficante, A., Girichidis, P., Glover, S.C.O., Smith, R.J., Sormani, M., Treß, R., 2022. The Galactic dynamics revealed by the filamentary structure in atomic hydrogen emission. *A&A* 662, A96. doi:10.1051/0004-6361/202243334, arXiv:2205.10426.

Sollima, A., Gil de Paz, A., Martinez-Delgado, D., Gabany, R.J., Gallego-Laborda, J.J., Hallas, T., 2010. A multi-wavelength analysis of M 81: insight on the nature of Arp's loop. *A&A* 516, A83. doi:10.1051/0004-6361/201014085, arXiv:1004.1610.

Stork, J.A., Spinello, L., Silva, J., Arras, K.O., 2012. Audio-based human activity recognition using non-markovian ensemble voting, in: 2012 IEEE RO-MAN: The 21st IEEE International Symposium on Robot and Human Interactive Communication, pp. 509–514. doi:10.1109/ROMAN.2012.6343802.

Szomoru, A., Guhathakurta, P., 1998. Optical Spectroscopy of Galactic Cirrus Clouds: Extended Red Emission in the Diffuse Interstellar Medium. *ApJ* 494, L93–L97. doi:10.1086/311156, arXiv:astro-ph/9712056.

Szomoru, A., Guhathakurta, P., 1999. Extinction curves, distances, and clumpiness of diffuse interstellar dust clouds,. *The Astronomical Journal* 117, 2226 – 2243. URL: <https://api.semanticscholar.org/CorpusID:15392082>.

Tang, P., Liang, Q., Yan, X., Zhang, D., Coppola, G., Multi-proportion, W.S., Alsup, A.M., Fowlds, K., Cho, M., Luber, J.M., BetaBuddy, 2023. Mobilenetv2 ensemble segmentation for mandibular on panoramic radiography. *International Journal of Intelligent Engineering and Systems* URL: <https://api.semanticscholar.org/CorpusID:257211721>.

Teeninga, P., Moschini, U., Trager, S., Wilkinson, M., 2016. Statistical attribute filtering to detect faint extended astronomical sources. *Mathematical Morphology - Theory and Applications* 1, 100–115. doi:10.1515/mathm-2016-0006.

Teeninga, P., Moschini, U., Trager, S.C., Wilkinson, M.H., 2013. Bi-variate statistical attribute filtering: A tool for robust detection of faint objects, in: 11th International Conference on Pattern Recognition and Image Analysis: New Information Technologies (PRIA-11-2013), pp. 746–749.

de Vaucouleurs, G., 1955. Emission nebulosities near the south pole. *The Observatory* 75, 129–130.

de Vaucouleurs, G., 1960. Emission nebulosities near the south pole - II. *The Observatory* 80, 106–109.

de Vaucouleurs, G., Freeman, K.C., 1972. Structure and dynamics of barred spiral galaxies, in particular of the Magellanic type. *Vistas in Astronomy* 14, 163–294. doi:10.1016/0083-6656(72)90026-8.

Vazquez-Semadeni, E., Gomez, G.C., Jappsen, A.K., Ballesteros-Paredes, J., Gonzalez, R.F., Klessen, R.S., 2007. Molecular cloud evolution. II. from cloud formation to the early stages of star formation in decaying conditions. *The Astrophysical Journal* 657, 870–883. URL: <https://doi.org/10.1086/510771>, doi:10.1086/510771.

Veneziani, M., Ade, P.A.R., Bock, J.J., Boscaleri, A., Crill, B.P., de Bernardis, P., De Gasperis, G., de Oliveira-Costa, A., De Troia, G., Di Stefano, G., Ganga, K.M., Jones, W.C., Kisner, T.S., Lange, A.E., MacTavish, C.J., Masi, S., Mauskopf, P.D., Montroy, T.E., Natoli, P., Netterfield, C.B., Pascale, E., Piacentini, F., Pietrobon, D., Polenta, G., Ricciardi, S., Romeo, G., Ruhl, J.E., 2010. Properties of Galactic Cirrus Clouds Observed by BOOMERANG. *ApJ* 713, 959–969. doi:10.1088/0004-637X/713/2/959, arXiv:0907.5012.

Vogelaar, M.G.R., Wakker, B.P., 1994. Measuring the fractal structure of interstellar clouds. *A&A* 291, 557–568.

de Vries, C.P., Le Poole, R.S., 1985. Comparison of optical appearance and infrared emission of some high latitude extended dust clouds. *A&A* 145, L7–L9.

de Vries, H.W., Heithausen, A., Thaddeus, P., 1987. Molecular and Atomic Clouds Associated with Infrared Cirrus in Ursa Major. *ApJ* 319, 723. doi:10.1086/165492.

Wang, S., Li, A., Jiang, B.W., 2015. Very Large Interstellar Grains as Evidenced by the Mid-infrared Extinction. *ApJ* 811, 38. doi:10.1088/0004-637X/811/1/38, arXiv:1508.03403.

Weiland, J.L., Blitz, L., Dwek, E., Hauser, M.G., Magnani, L., Rickard, L.J., 1986. Infrared Cirrus and High-Latitude Molecular Clouds. *ApJ* 306, L101. doi:10.1086/184714.

Weingartner, J.C., Draine, B.T., 2001. Dust grain-size distributions and extinction in the milky way, large magellanic cloud, and small magellanic cloud. *The Astrophysical Journal* 548, 296 – 309. URL: <https://api.semanticscholar.org/CorpusID:121359249>.

Witt, A.N., Friedmann, B.C., Sasseen, T.P., 1997. Radiative Transfer Analysis of Far-Ultraviolet Background Observations Obtained with the Far Ultraviolet Space Telescope. *ApJ* 481, 809–820. doi:10.1086/304093, arXiv:astro-ph/9701017.

Witt, A.N., Mandel, S., Sell, P.H., Dixon, T., Vijh, U.P., 2008. Extended Red Emission in High Galactic Latitude Interstellar Clouds. *ApJ* 679, 497–511. doi:10.1086/587131, arXiv:0802.0674.

Wolf, M., 1923. Über den dunklen Nebel NGC 6960. *Astronomische Nachrichten* 219, 109. doi:10.1002/asna.19232190702.

Yin, X., Chen, W., Wu, X., Yue, H., 2017. Fine-tuning and visualization of convolutional neural networks, in: 2017 12th IEEE Conference on Industrial Electronics and Applications (ICIEA), pp. 1310–1315. doi:10.1109/ICIEA.2017.8283041.

Zavagno, A., Dupé, F.X., Bensaid, S., Schisano, E., Li Causi, G., Gray, M., Molinari, S., Elia, D., Lambert, J.C., Brescia, M., Arzoumanian, D., Russeil, D., Riccio, G., Cavuoti, S., 2023. Supervised machine learning on Galactic filaments. Revealing the filamentary structure of the Galactic interstellar medium. *A&A* 669, A120. doi:10.1051/0004-6361/202244103, arXiv:2212.00463.

Zeraatgari, F.Z., Hafezianzadeh, F., Zhang, Y., Mei, L., Ayubinia, A., Mosallanezhad, A., Zhang, J., 2024. Machine learning-based photometric classification of galaxies, quasars, emission-line galaxies, and stars. *MNRAS* 527, 4677–4689. doi:10.1093/mnras/stad3436, arXiv:2311.02951.

Zhang, J., Martin, P.G., Cloutier, R., Price-Jones, N., Abraham, R., van Dokkum, P., Merritt, A., 2023. Joint Modelling of Dust Scattering and Thermal Emission: The Spider Complex. *ApJ* 948, 4. doi:10.3847/1538-4357/acc177, arXiv:2305.00756.

Zhao, Y., Zhang, W., Ma, L., Wen, S., Wu, H., 2024. Galactic Cirri at High Galactic Latitudes. I. Investigating Scatter in Slopes between Optical and Far-infrared Intensities. *AJ* 168, 88. doi:10.3847/1538-3881/ad58d5, arXiv:2406.03031.

Zhou, Z., Siddiquee, M.M.R., Tajbakhsh, N., Liang, J., 2018. Unet++: A nested u-net architecture for medical image segmentation. Deep Learning in Medical Image Analysis and Multimodal Learning for Clinical Decision Support : 4th International Workshop, DLMIA 2018, and 8th International Workshop, ML-CDS 2018, held in conjunction with MICCAI 2018, Granada, Spain, S... 11045, 3–11. URL: <https://api.semanticscholar.org/CorpusID:50786304>.

Zubko, V., Dwek, E., Arendt, R.G., 2004. Interstellar dust models consistent with extinction, emission, and abundance constraints. *The Astrophysical Journal Supplement Series* 152, 211–249. URL: <https://doi.org/10.1086/382351>. doi:10.1086/382351.